Lawrence Berkeley National Laboratory
LBL Publications

Title
Stochastic Ion Heating by Lower Hybrid Turbulence

Permalink
https://escholarship.org/uc/item/986140xc

Author
Candy, J

Publication Date
1990-05-01

Lawrence Berkeley Laboratory
UNIVERSITY OF CALIFORNIA

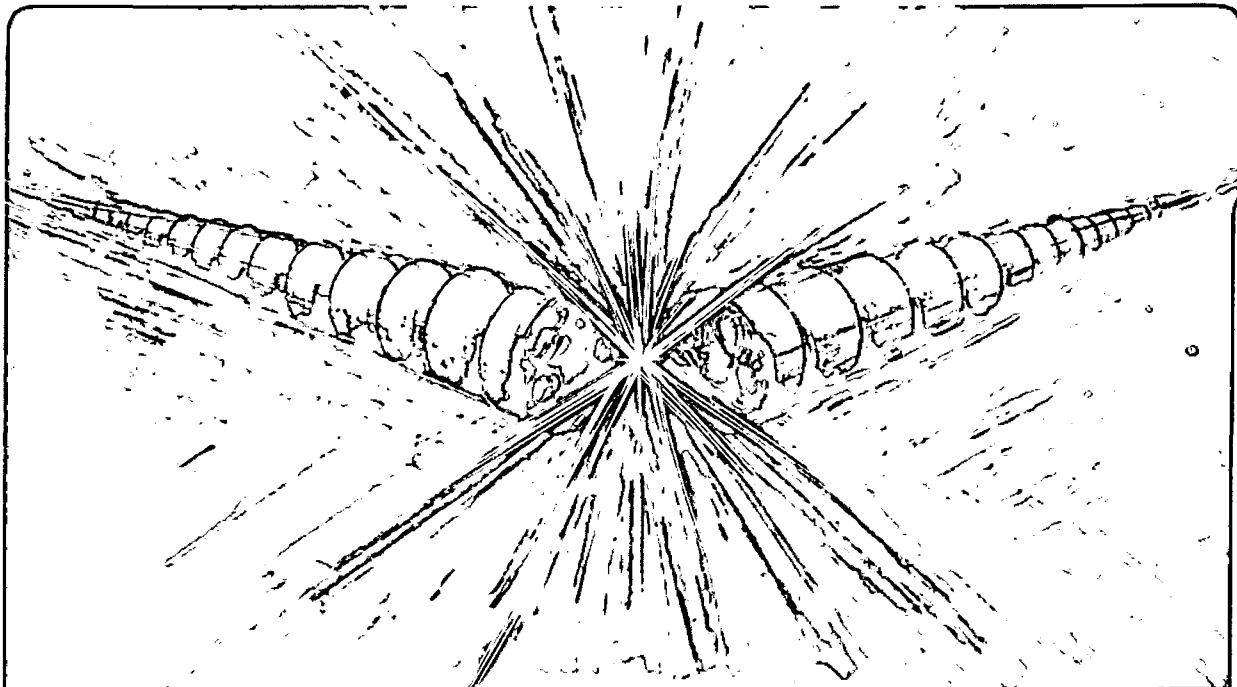## Accelerator & Fusion
Research Division

**Stochastic Ion Heating by
Lower Hybrid Turbulence**

J. Candy

May 1990

DISCLAIMER

STOCHASTIC ION HEATING BY LOWER HYBRID TURBULENCE*

J. Candy+

Exploratory Studies Group
Accelerator & Fusion Research Division
Lawrence Berkeley Laboratory
1 Cyclotron Road
Berkeley, CA 94720

May 1990

+ Permanent Address: Dept. of Physics, University of Alberta,
Edmonton, Alberta, Canada T6G 2G1

STOCHASTIC ION HEATING BY LOWER HYBRID TURBULENCE

J. Candy

Abstract

The motion of an ion in a spectrum of lower hybrid waves propagating across a constant magnetic field is examined. In particular, numerical simulation is used to determine the extent to which a turbulent spectrum of these electrostatic waves may accelerate thermal ions ($T < 1$ eV). The significance of stochastic web development in this heating process is also discussed.

1 Introduction

Consider a particle with mass m and charge e gyrating in a uniform magnetic field $B\hat{z}$ and interacting with an electrostatic wave. The magnetic field in this case may be derived from the vector potential $\mathbf{A} = Bx\hat{y}$. Then, if the wave has amplitude E and spatial frequency ω, the Hamiltonian of the particle can be written as

$$H = \frac{1}{2m}\left[(m\Omega x)^2 + p_x^2 + p_z^2\right] + \frac{eE}{k}\cos(k_x x + k_z z - \omega t), \qquad (1)$$

where $\Omega \equiv eB/m$ is the cyclotron frequency. Note that we have chosen the wavevector $\mathbf{k} = k_x\hat{x} + k_z\hat{z}$ to lie in the x-z plane. That this results in no loss of generality should be clear.

The Hamiltonian (1) has been studied in some detail by Smith and Kaufman [1], [2]. By considering the overlap of adjacent resonances, these authors obtained a crude estimate of the onset of global stochasticity according to the well-known Chirikov criterion.

More detailed studies, however, have involved a simplified version of (1). If one considers the wave to propagate transversely ($k_z = 0$), then the previous Hamiltonian function reduces to

$$H = \frac{1}{2m}\left[(m\Omega x)^2 + p_x^2\right] + \frac{eE}{k}\cos(kx - \omega t). \qquad (2)$$

This Hamiltonian has been examined in the context of particle heating by a lower hybrid wave – the propagation of which is characterized by $k_x \gg k_z$ and $\omega \gg \Omega$. Fukuyama *et al.* [3] have analysed (2) in the case where ω is an integer multiple of Ω, while Karney [4] has considered the more general case of arbitrary wave frequency. Futhermore, Karney has also extended some of the interesting results obtained for (2) to the more general Hamiltonian (1). Malkov [5] and Zaslavsky *et al.* [6], finally,

have studied the equations of motion which result from (2) in the presence of an arbitrarily weak magnetic field.

More recently, much attention has been given to the interesting dynamics which occur when $\omega/\Omega \in \mathbb{Z}$. In this resonant case, the phase space of the system is covered by a stochastic web. Some interesting properties of the separatrix mesh were shown by Chernikov *et al.* [7] for one wave, and numerically by Murakami *et al.* [8] for up to 20 waves. In addition, Karimabadi and Angelopoulos [9] – using first order perturbation theory – have studied invariant curves in phase space for the interaction of a relativistic particle with an obliquely propagating wave packet of arbitrary polarization. They point out certain limitations and weaknesses associated with the usual nonrelativistic treatment.

Finally, by considering a wave packet composed of an infinite number of modes uniformly spaced in frequency, Zaslavsky *et al.* [10] were able to construct an exact mapping from the continuous Hamiltonian. The iterates of this mapping generate a web with remarkable symmetry properties and fractal-like structure. In fact, the geometry of the separatrix mesh in phase space is reminiscent of a Penrose tiling (see [11], [12]). An interesting summary of stochastic webs in general may be found in [13]. Unfortunately, the structure of the electric fields which give rise to such interesting dynamics are often difficult to justify from a physical standpoint.

2   A Model of Lower Hybrid Turbulence

Particle heating in the earth's ionosphere is believed to result from the interaction of ions with lower hybrid waves. (see [14] and [15]). In particular, precipitating electron beams in this region of the ionosphere might constitute a natural free energy source for the generation of lower hybrid waves. Unfortunately, the general problem of particle heating is enormously complicated, and it is no surprise that many aspects of these processes are still poorly understood. In what follows, we will investigate a single particle model of heating which is similar in form to, but slightly more general than the system (2). Further, we will examine the behavior of our model using physical parameters which are believed to be characteristic of a plasma containing such lower hybrid waves.

2.1   The Model Hamiltonian

To begin with, we consider a spectrum of N transversely propagating electrostatic waves. This case is a simple generalization of (2), with the electric field now described by the wave packet

$$E(x,t) = \sum_{i=1}^{N} E_i \sin(k_i x - \omega_i t + \varphi_i). \tag{3}$$

The Hamiltonian for a particle subject to this more general electric field can be written

$$\mathcal{H} = \frac{1}{2}(x^2 + p^2) + \sum_{i=1}^{N} \frac{\epsilon_i}{k_i} \cos(k_i x - \nu_i T + \varphi_i). \tag{4}$$

Note that we have introduced the dimensionless time $T \equiv \Omega t$ and the canonical momentum $p \equiv dx/dT = p_x/m\Omega$, so that $\mathcal{H}$ has dimensions of (length)^2. The parameter ν_i is related to the temporal frequency ω_i of the ith wave by the relationship

$$\nu_i \equiv \frac{\omega_i}{\Omega}.$$

3

Furthermore, for a plasma composed of singly ionized hydrogen, the nonlinearity parameter ϵ_i is defined in terms of the mode amplitude E_i according to

$$\epsilon_i \equiv \frac{eE_i}{m_p\Omega^2}. \tag{5}$$

Also, in each wave we have included an arbitrary phase factor φ_i which can be set to any value in the range $0 \leq \varphi_i < 2\pi$. In principle, all that remains is to choose reasonable values for the parameters ϵ_i, k_i, ν_i and Ω so that the equations of motion corresponding to (4) may be solved numerically.

2.2 Limiting the Parameter Space

At altitudes between 500 km and 2500 km the background magnetic field varies from about 4×10^{-5} Tesla to 2×10^{-5} Tesla. In general, we will assume that B assumes a constant value of

$$B = 4 \times 10^{-5} \text{ Tesla, so that } \Omega = 3.8318 \times 10^3 \text{ s}^{-1},$$

corresponding to a lower altitude field strength. Typical measured electric field amplitudes are on the order of 0.01 V/m [16]. Significantly higher amplitudes are indeed possible, and we consider (arguably high) maximum values on the order of 1 V/m for $E(x, t)$. This implies that the normalized maximum value of the field (see (5)) is

$$\frac{eE(x, t)}{m_p\Omega^2} \sim 10 \text{ m}.$$

(Actually, we will consider this to be an upper bound on the RMS value of the normalized field. This is discussed at length in Section 3.3). Such a restriction provides a rough guideline for choosing the set of nonlinearity parameters ϵ_i.

Next, to decide upon a reasonable value for each ν_i we must make use of the

4

dispersion relation for LH waves:

$$\omega = \omega_{pi}\left(1 + \frac{\omega_{pe}^2}{\omega_{ge}^2}\right)^{-1/2}\left(1 + \frac{m_p}{m_e}\sin^2\theta\right)^{1/2}, \tag{6}$$

where

$$\omega_{pi}^2 = \frac{n_0 e^2}{\varepsilon_0 m_p}, \quad \omega_{pe}^2 = \frac{n_0 e^2}{\varepsilon_0 m_e}, \quad \omega_{ge}^2 = \frac{B^2 e^2}{m_e},$$

and $\tan\theta = k_z/k_x$. These expressions show the explicit dependence of ω on the local density n_0.

The dispersion relation (6) is valid for small θ (i.e., $k_z \ll k_x$). Also, it is true that the Hamiltonian (4) – to a good approximation – describes the ion motion in the x-y plane even for small but nonzero k_z. Of course, the price of this simplification is to forego any detailed knowledge of the parallel motion. Fortunately, our concern here is with perpendicular acceleration only, so that this loss of information is of little concern. As a result, (4) affords us a valid picture of the perpendicular motion even beyond the $k_z = 0$ approximation.

Upon dividing (6) by Ω and squaring the result, one obtains

$$\left(\frac{\omega}{\Omega}\right)^2 = m_p\left(\frac{\varepsilon_0 B^2}{n_0} + m_e\right)^{-1}\left(1 + \frac{m_p}{m_e}\sin^2\theta\right). \tag{7}$$

In the region of the ionosphere we are interested in, realistic densities range from 10^8 m^{-3} to 10^{10} m^{-3}. Then, according to (7), the interval $0 \le \theta \le \pi/60$ corresponds to the following ranges in ω/Ω:

$$3.4 \le \frac{\omega}{\Omega} \le 8.4 \quad \text{for} \quad n_0 = 10^8 \text{ m}^{-3},$$

$$26.8 \le \frac{\omega}{\Omega} \le 65.8 \quad \text{for} \quad n_0 = 10^{10} \text{ m}^{-3}.$$

Using these limits as rough guidelines, we assume that ν_i may lie anywhere in the range

$$4 \le \nu_i \le 30.$$

It remains to find a physically reasonable value for each wavenumber k_i. Unfortunately, no physical measurements of the wavevectors of ionospheric lower hybrid waves have been obtained. It seems the best we can do is to consider possible driving sources of the waves, and derive a theoretical estimate. According to Koskinen [16], values of k_i on the order of 1 m^{-1} may be obtained by assuming that the LH waves are excited by a parallel beam of 4-keV electrons. Hence, we assume each k_i is restricted to the interval

$$0.1 \text{ m}^{-1} \leq k_i \leq 1.0 \text{ m}^{-1}.$$

2.3   Initial Conditions of Source Ions

Using the canonical variables we defined earlier, the ion gyroradius ρ, defined by

$$\rho^2 \equiv \frac{1}{\Omega^2} \left[\left(\frac{dx}{dt} \right)^2 + \left(\frac{dy}{dt} \right)^2 \right],$$

takes on the simple form

$$\rho = \sqrt{p^2 + x^2}. \tag{8}$$

To see this, one must realize that in the derivation of (1), p_y was chosen to have a constant initial value of zero, thus implying

$$p_y = m \frac{dy}{dt} + m\Omega x = 0.$$

The perpendicular kinetic energy (or temperature) T of a test ion is, of course, related to the square of the gyroradius by

$$T = \frac{m_p}{2e} (\Omega \rho)^2 \quad \text{[in eV]}.$$

Typical ionospheric source ions have kinetic energies on the order of a fraction of an eV [14]. Let us assume that the ions we are considering have, in their perpendicular degrees of freedom, kinetic energies between 0.25 eV and 1 eV. This range

in energy corresponds corresponds to gyroradii in the interval

$$1.8 \text{ m} \leq \rho \leq 3.6 \text{ m}.$$

2.4 Method of Integration

To study the time evolution of p and x, we can generate a symplectic integration algorithm using the Hamiltonian function (4). Specifically, we will use the SIA4 algorithm derived in [17]. This algorithm is accurate to 4th order in the time step, and is one of a class of symplectic integrators devised originally by Ruth [18], [19]. With (4) written in the form $\mathcal{H} = \mathcal{H}_1(p) + \mathcal{H}_2(x, T)$, the SIA uses the functions

$$F(x, T) \equiv -\partial_x \mathcal{H}_2(x, T) = \sum_{i=1}^{N} \epsilon_i \sin(k_i x - \nu_i T + \varphi_i) - x$$

and

$$P(p) \equiv \partial_p \mathcal{H}_1(p) = p$$

to construct an explicit, analytic symplectic map. This symplectic map approximates the exact phase flow induced by $\mathcal{H}$, accurate to fourth order in the time step. The advantages of using SIA4 in place of a more common non-symplectic integrator are many, and are discussed at length in [17]. Further details concerning the integration procedure will be discussed later.

7

3 Numerical Results

Using the SIA4 algorithm, we studied the time development of our model system for a variety of parameter values. A discussion of the results of this study appears below, with a separate section devoted to each particular simulation. Furthermore, a collection of figures which summarize the respective simulations appears at the end of this paper, supplemented by captions which describe in full the associated parameter spaces.

The time steps δT used in SIA4 had the form

$$\delta T = \frac{\Delta T}{j}, \quad \text{where} \quad \Delta T \equiv \frac{2\pi}{\bar{\nu}}. \tag{9}$$

In the above,

$$\bar{\nu} \equiv \{\text{the integer nearest to } \max(\nu_1, \ldots, \nu_N)\},$$

and j is an arbitrary integer characterizing the smallness of the time step – and hence the accuracy of the symplectic integrator. Generally, j was chosen to lie between about 20 and 25; a size at which, loosely speaking, it is probably valid to forget about the original Hamiltonian and consider the system as described exactly by the symplectic map SIA4.

3.1 Heating with One Mode

3.1.1 Surfaces of Section

We begin by studying the time evolution of a system corresponding to the Hamiltonian (4) for the simplest case of $N = 1$. Figures 1 and 2 illustrate the structure of phase space for this case, with all parameters equal except for ν_1. In particular, the first figure has $\nu_1 = 5$, while the second has $\nu_1 = 5.16$. In both cases, the wave

amplitudes are relatively small, leaving much of the phase space covered by invariant tori. However, the two cases have clearly distinct topologies. In the first case, there exists a narrow channel of interconnected separatrices which form a web that spans the entire phase plane. This is in contrast to the picture in Figure 2, which displays a series of nested tori as predicted by the KAM theorem. Interestingly, the violation of the KAM theorem in the first case, as a consequence of ν_1 being an integer, allows a theoretical diffusion along the stochastic network to arbitrarily large energies. However, the thickness of the web decreases rapidly with increasing velocity, so that diffusion is quite limited in practice.

Next, Figures 3 and 4 illustrate the effect of increasing the strength of the electrostatic wave. By comparing Figure 3 to Figure 1, it becomes clear that the increase in wave amplitude produces a widening of the stochastic network, while in Figure 4, one can see that it leads to a breakup of invariant tori. Finally, a characteristic common to all of these first four figures is the existence of a sequence of little tori enclosing the origin which effectively trap low energy particles. We will comment on the significance of such barriers in inhibiting particle acceleration later.

3.1.2 Ensemble Averaging

Next, we wish to examine the average phase space population $N(\rho)$ which results from accelerating an ensemble of low energy particles using the Hamiltonian (4). The steps taken to determine this quantity are described below:

- Assign 10 ions random positions in the phase space annulus $1.8 \text{ m} \leq \rho \leq 3.6 \text{ m}$ at $T = 0$.

- Integrate each particle in this ensemble forward in time to $T = 200\pi$.

- From $T = 200\pi$ to $T = 2000\pi$, record the position of each particle at successive time intervals $\Delta T = 2\pi/\bar{\nu}$ (see (9)).

Figures 4 through 9 illustrate this averaging procedure for fixed values of ν_1, k_1 and φ_1, but with successively increasing wave amplitude ϵ_1. In the figures, $N(\rho)$ is expressed in arbitrary units. The local depletion of particles in each case corresponds to the presence of large first-order islands such as those in Figure 1. In the limit of small wave amplitude, the elliptic fixed points exist at gyroradii ρ which satisfy

$$J'_{\nu_1}(k_1\rho) = 0.$$

As the wave amplitude grows to its maximum value, successive elliptic points are encircled, while the distributions around previous fixed points become smeared as invariant curves are destroyed.

The same simulation, with $\nu_1 = 5.16$, exhibits essentially no growth in energy. This can be seen in Figures 10 and 11, and results from the entire ensemble remaining trapped by invariant tori.

However, the situation changes if we double the wavevector k_1 to unity. Figure 12 ($\nu_1 = 5$) and Figure 13 ($\nu_1 = 5.16$) illustrate the results of a simulation which considered only one ion averaged over the period $T = 200\pi$ to $T = 6000\pi$, with ΔT defined as before. These results show comparable heating profiles for both values of ν_1. The increased magnitude of k_1 effectively reduces the phase velocity of each wave and, in the case of noninteger ν_1, destroys tori closer to the origin and allows stochastic diffusion of the test ion.

10

3.2 Amplitudes of Ordered and Turbulent Wave Spectra

We claimed in Section 2.2 that the normalized maximum value of the electric field should not exceed roughly 10 m. We did not, however, put particular restrictions on the normalized mode amplitudes ϵ_i. Clearly, the maximum possible amplitude of a wave packet composed of N sinusoidal modes, each with amplitude ϵ_i, is simply

$$\sum_{i=1}^{N} | \epsilon_i | . \tag{10}$$

However, in reality, one would expect that such an amplitude would rarely be attained – especially in the case where N is large.

Consider, first, the normalized electric field seen by the particle at time T:

$$\mathcal{E}(x(T), T) \equiv \frac{eE(x(T), T)}{m_p \Omega^2} = \sum_{i=1}^{N} \epsilon_i \sin(k_i x(T) - \nu_i T + \varphi_i). \tag{11}$$

The RMS value of this field, taken over time interval $[0, \tau]$, is defined as

$$\mathcal{E}_{rms}(\tau) \equiv \left[\frac{1}{\tau} \int_0^\tau \mathcal{E}^2(x(T), T) dT \right]^{1/2}. \tag{12}$$

In the limit $k_i \to 0$, and $\tau \to \infty$, it is simple to calculate $\mathcal{E}_{rms}$ analytically. Calling this limiting value of the RMS field $\tilde{\mathcal{E}}_{rms}$, it is easy to show that

$$\tilde{\mathcal{E}}_{rms} = \left[\frac{1}{2} \sum_{i=1}^{N} \epsilon_i^2 \right]^{1/2}. \tag{13}$$

The validity of this result also requires that all ν_i are distinct.

We numerically computed $\mathcal{E}_{rms}(10\pi/\nu_{min})$ for two different wave packets, each with $N = 10$, and compared the results with the approximate value $\tilde{\mathcal{E}}_{rms}$. The first case, shown in Figure 14, consists of waves evenly spaced in frequency with constant wavenumber and amplitude. The reader should recognize this spectrum as one which will give rise to a stochastic web. It happens that $\mathcal{E}_{rms}$ for this ordered packet is 2.2 m – in close agreement with $\tilde{\mathcal{E}}_{rms} = \sqrt{5}$ m $\simeq 2.236$ m. It is interesting

11

to note that as $N \rightarrow \infty$ in such a packet, the electric field seen by the particle approaches a periodic comb of delta functions, and is then described by the mapping of Zaslavsky, *et al.* [10]. In fact, such periodic impulses, or "kicks", seem to be a generic aspect of chaos in Hamiltonian systems. Potential fields of this type give rise to many popular 2-D symplectic maps of the plane which are known to be chaotic – the *Standard and Fermi Maps*, for example. Furthermore, various approximate analyses of (2) ([5], for example) have concentrated on constructing a perturbed twist map of the plane which replaces the exact motion by: (i) a kick at $\dot{x} = \omega/k$, and (ii) unperturbed linear oscillation everywhere else, as shown in Figure 31. In a qualitative sense, it can be claimed that if the kick is strong enough, the particle will undergo a substantial phase change which will lead to stochastic motion. For this reason, it seems that the study of finite and infinite mode stochastic webs may be useful from the point of view of understanding the generic aspects of particle heating in the ionosphere.

In any case, we also calculated $\mathcal{E}_{rms}(10\pi/\nu_{min})$ for the turbulent spectrum shown in Figure 15. While the structure of the field is much more erratic in this case than in the last, the value $\mathcal{E}_{rms} = 2.3$ m is quite comparable.

These calculations provides us with a rough estimate of the relationship between (10) and $\mathcal{E}_{rms}$, and serve to justify the values of ϵ_i used in the multiple mode simulations which follow.

3.3 Multiple Mode Stochastic Webs

As we mentioned in the last section, the study of finite mode stochastic webs may contribute to a better understanding of certain general properties of ionospheric particle heating. With this in mind, we choose to examine three particular cases, each for realistic values of the various wave parameters. Before doing so, we remind

the reader of some fundamental ideas in nonlinear dynamics.

First, it has been shown that when the number of degrees of freedom satisfies $n \geq 3$, a separatrix net may arise which extends throughout phase space. This net, which was predicted by Arnold, forms a stochastic web along which particles may wander chaotically. The name given to this motion is *Arnold diffusion*, and results from the intersection of invariant tori which do not divide phase space (since $n \geq 3$). However, the Hamiltonian (4) represents only $n = 3/2$ degrees of freedom, thus showing (see Figures 16 to 18) that an Arnold-type diffusion may occur even in the case of minimal dimension for nonintegrability.

3.3.1 Four Modes

Shown in Figure 16 is the stochastic web which results from a wave packet composed of four modes. The frequencies are spaced according to $\nu_i = 5i$ for $i = 1, \ldots, 4$; while the amplitudes and wavevectors are constant. Interestingly, the particle spent most of its time sticking to the tori centered at $\rho \sim 38$ m, and consequently the iterates were distributed very nonuniformly in phase space.

3.3.2 Five Modes

Next, we consider five modes with equal amplitude, and frequencies which are multiples of 5 – but not spaced as in the last example. In this case, we vary the wavenumber so that waves with equal values of ν_i will have different phase velocities. The effect of this modification is shown in Figure 17. We see quite dramatic heating effects, with gyroradii approaching 110 m (or energies approaching 0.93 keV). This is achieved, however, with relatively low amplitude RMS fields (less than 0.5 V/m), and in the *absence* of what is normally considered to be global stochasticity (i.e., destruction of nearly all invariant tori).

3.3.3 Six Modes

As a final example of stochastic web heating, we add a sixth mode to the previous system. This has the effect, surprisingly, of limiting the maximum energy gain to only about 0.62 keV (see Figure 18). Unfortunately, the tendency of the iterates on the surface of section to explore some areas of the separatrix mesh and not others is marked by a sensitive dependance on both initial conditions and the maximum integration time T_{max}. In instances of very large T_{max}, the areas of the web which are explored also depend on the time step used in SIA4 and on the precision of all floating point operations.

3.4 Heating by a Completely Turbulent Spectrum

This final series of simulations is aimed at modeling particle heating in a "realistic" spectrum of waves. We consider $N = 10$ waves, each with normalized frequency ν_i, wavenumber k_i and phase φ_i chosen at random inside the intervals described in Section 2.2. Then, we calculate the average population $N(\rho)$ according to the prescription in Section 3.1.2 for various cases characterized by different values of the ϵ_i. We performed 12 separate runs, which had the collective structure shown in Table 1. For the 6 runs labeled by "A", we chose the wave parameters

$$\left\{ \nu_i^{(A)}, k_i^{(A)}, \varphi_i^{(A)} \right\}_{i=1}^{10},$$

which remained constant for all values of the mode amplitudes. Then, for each A run, we chose a set of mode amplitudes (composed of 10 ϵ_i) at random in the interval $[\epsilon_{min}, \epsilon_{max}]$. For the runs labeled "B", we generated new values for the wave parameters and the initial ion distribution, then performed the simulations with the same mode amplitudes as in the A runs. The maximum gyroradius ρ_{max}

and corresponding temperature T_{max} to which the ions were accelerated also appear in Table 1. The distributions $N(\rho)$ appear in Figures 19 to 30.

Each of these simulations was performed on a CRAY X-MP supercomputer, using single precision real variables (14 digit accuracy). The integrator time step was chosen with $j = 25$ (see (10)).

Perhaps the first difference which one notices in the heating profiles is the value of ρ_{max} in runs 1B, 2B and 3B; it is significantly lower than in the corresponding A runs. This can be explained, however, in terms of the minimum modal phase velocities. The slowest modes in the A and B runs respectively had normalized phase velocities of

$$\left\{ \frac{\nu_i^{(A)}}{k_i^{(A)}} \right\}_{min} \simeq 5.57 \text{ m} \quad \text{and} \quad \left\{ \frac{\nu_i^{(B)}}{k_i^{(B)}} \right\}_{min} \simeq 7.56 \text{ m}.$$

Now, for a particle to be effectively accelerated by a wave, it must be moving with a velocity *not* substantially less than the phase velocity of that wave. Otherwise, as seen in Figure 31, no resonant interaction will occur. This effect is manifested in our simulation, where the faster moving B wave is less effective at providing the first jolts of acceleration than the slower A wave. This is one aspect of particle acceleration, however, that is greatly enhanced by the presence of a stochastic web. Because of the large first-order islands created by resonance, particles which are initially located close to the origin in phase space ($T < 1$ eV) may be swept out to substantially higher energies than would be possible otherwise. This is seen clearly in Figure 1, where the separatrix mesh which surrounds the first-order islands reaches very close to the origin. This effect is not observed in Figure 2, where the invariant tori divide the phase space into successive annulus-like regions.

Next, it happens that the maximum velocity to which a particle may be accelerated is also dependent upon the values of the modal phase velocities. To see

this, note that in the A and B runs respectively, the maximum normalized phase velocities were

$$\left\{\frac{\nu_i^{(A)}}{k_i^{(A)}}\right\}_{max} \simeq 92.2 \text{ m} \quad \text{and} \quad \left\{\frac{\nu_i^{(B)}}{k_i^{(B)}}\right\}_{max} \simeq 67.2 \text{ m}.$$

The larger phase velocity in case A allows stochastic diffusion to occur at correspondingly larger gyroradii. As a result, for the maximum electric field amplitudes in runs 6A and 6B, case A exhibits superior particle heating characteristics.

3.5 The Disappearance of Landau Damping

Recall that one may define the *dielectric response function* $\varepsilon(\mathbf{k}, \omega)$ of a plasma in terms of the dielectric tensor $\epsilon(\mathbf{k}, \omega)$ according to

$$\varepsilon(\mathbf{k}, \omega) \equiv \frac{\mathbf{k} \cdot \epsilon(\mathbf{k}, \omega) \cdot \mathbf{k}}{k^2}. \tag{14}$$

For a plasma in a uniform, external magnetic field such as that pertaining to (1), we can write this response as a sum over all ion species σ according to [20]

$$\varepsilon(\mathbf{k}, \omega) = 1 - \sum_{\sigma} \sum_{n=-\infty}^{\infty} \int d^3v \, \frac{F_{\sigma,n}(\mathbf{v})}{n\Omega_\sigma + k_z v_z - \omega - i\eta}. \tag{15}$$

The explicit form of $F_{\sigma,n}(\mathbf{v})$, which is not important for our purposes, is determined by the single-particle velocity distribution function $f_\sigma(\mathbf{v})$. When the wave propagates obliquely to the magnetic field, the contributions to the response occur at values of v_z where the denominator in the integral vanishes. These resonances, of course, are the sources of *linear Landau damping* of the plasma wave. However, if we let the wave propagate transversely to the magnetic field as in (2), then the new set of resonances $\omega = n\Omega_\sigma$ are independent of $\mathbf{v}$ – and the Landau damping vanishes. This phenomenon has been examined closely in [5] and [6], where it is shown that the paradoxical disappearance of Landau damping is accompanied by

16

the emergence of a particular form of nonlinear damping. This new damping is related to the stochastic instability of particle motion. In particular, stochastic web formation is one example of this phenomenon.

Conclusion

If lower hybrid waves are indeed responsible for the bulk heating of ions in the ionosphere, we hope that the simulations described herein might help elucidate some of details of the wave-particle interactions involved. Indeed, by studying this simple single particle model, we can gain a better understanding of the characteristics and limitations of LH heating.

Unfortunately, as was mentioned earlier on, the processes which we have tried to model in this paper are still quite poorly understood. Further, lower hybrid heating is by no means the only possible mechanism for ion acceleration in the suprauroral region. While the upper limit of $T_{max} \sim 1$ keV (at RMS fields of roughly 1.2 V/m) is of the same order of magnitude as temperatures of observed hot ions populations, more experimental data is needed before researchers are able to construct a truly reliable picture of these ionospheric processes.

Acknowlegments

References

[1] G. R. Smith and A. N. Kaufman, Phys. Rev. Lett. **34** (1975) 1613.

[2] G. R. Smith and A. N. Kaufman, Phys. Fluids **21** (1978) 2230.

[3] A. Fukuyama, H. Momota, R. Itatani and T. Takizuka, Phys. Rev. Lett. **38** (1977) 701.

[4] C. F. F. Karney, Phys. Fluids **21** (1978) 1584; **22** (1979) 2188.

[5] M. A. Malkov and G. M. Zaslavsky, Phys. Lett. **106A** (1984) 257.

[6] G. M. Zaslavsky, M. A. Malkov, R. Z. Sagdeev and V. D. Shapiro, Sov. J. Plasma Phys. **12**(7) (1986) 453.

[7] A. A. Chernikov, M. Ya. Natenzon, B. A. Petrovichev, R. Z. Sagdeev and G. M. Zaslavsky, Phys. Lett. **122A** (1987) 39.

[8] S. Murakami, T. Sato and A. Hasegawa, Physica D, **32** (1988) 259.

[9] H. Karimabadi and V. Angelopoulos, Phys. Rev. Lett. **62** (1989) 2342.

[10] G. M. Zaslavsky, M. Yu. Zakharov, R. Z. Sagdeev, D. A. Usikov and A. A. Chernikov, Sov. Phys. JETP **64**(2) (1986) 294.

[11] N. N. Filonenko, R. Z. Sagdeev and G. M. Zaslavsky, Nuclear Fusion 7 (1967) 253.

[12] A. J. Lichtenberg and B. P. Wood, Phys. Rev. **39**, (1989) 2153.

[13] A. A. Chernikov, R. Z. Sagdeev, D. A. Usikov, M. Yu. Zakharov and G.M. Zaslavsky, Nature **326** (1989) 559.

[14] G B. Crew and T. Chang, in: Physics of Space Plasmas (1985-87), eds. T. Chang, J. Belcher, J. R. Jasperse and G. B. Crew, SPI Conf. Proc. and Reprint Series, vol. 6 (Scientific Publishers, Cambridge, MA, 1987) p. 55.

[15] T. Chang, G. B. Crew and J. M. Retterer, Computer Physics Communications **49** (1988) 61.

[16] H. E. Koskinen, J. Geophys. Res., 90 (1985) 8361.

[17] J. Candy and W. Rozmus, accepted for publication in J. Comput. Phys.

[18] R. D. Ruth, IEEE Trans. Nucl. Sci., NS-30, (1983) 2669.

[19] E. Forest and R. D. Ruth, accepted for publication in Physica D.

[20] S. Ichimaru, *Basic Principles of Plasma Physics*, (Benjamin/Cummings, Reading, Mass. 1973) p. 51–59.

Figure Captions

1. Surface of section of the Hamiltonian (4) for $N = 1$. The wave parameters are $\epsilon_1 = 0.7$ m, $\nu_1 = 5$, $k_1 = 1$ m^{-1} and $\varphi_1 = 0$. Points are plotted at the times $T_p = 2\pi p/\nu_1$. Trajectories corresponding to various initial conditions are plotted, and the integration parameter j is 20.

2. Same as [1], except $\nu_1 = 5.16$.

3. Surface of section of the Hamiltonian (4) for $N = 1$. The wave parameters are $\epsilon_1 = 1.75$ m, $\nu_1 = 5$, $k_1 = 1$ m^{-1} and $\varphi_1 = 0$. Points are plotted at the times $T_p = 2\pi p/\nu_1$. Trajectories corresponding to various initial conditions are plotted, and the integration parameter j is 20.

4. Same as [3], except $\nu_1 = 5.16$.

5. Time-averaged ion distribution $N(\rho)$ versus gyroradius ρ for the Hamiltonian (4). Ten ions in the field of a single ($N = 1$) wave are averaged over the interval $200\pi \leq T \leq 2000\pi$. The wave parameters are $\epsilon_1 = 1$ m, $\nu_1 = 5$, $k_1 = 0.5$ m^{-1} and $\varphi_1 = 0$, and the integration parameter j is 25.

6. Same as [5], except $\epsilon_1 = 1.5$ m.

7. Same as [5], except $\epsilon_1 = 2$ m.

8. Same as [5], except $\epsilon_1 = 2.5$ m.

9. Same as [5], except $\epsilon_1 = 3$ m.

10. Time-averaged ion distribution $N(\rho)$ versus gyroradius ρ for the Hamiltonian (4). Ten ions in the field of a single ($N = 1$) wave are averaged over the

interval $200\pi \leq T \leq 2000\pi$. The wave parameters are $\epsilon_1 = 1$ m, $\nu_1 = 5.16$, $k_1 = 0.5$ m^{-1} and $\varphi_1 = 0$, and the integration parameter j is 25.

11. Same as [10], except $\epsilon_1 = 3$ m.

12. Time-averaged ion distribution $N(\rho)$ versus gyroradius ρ for the Hamiltonian (4). One ion in the field of a single ($N = 1$) wave is averaged over the interval $200\pi \leq T \leq 6000\pi$. The wave parameters are $\epsilon_1 = 3$ m, $\nu_1 = 5$, $k_1 = 1$ m^{-1} and $\varphi_1 = 0$, and the integration parameter j is 20.

13. Same as [12], except $\nu_1 = 5.16$.

14. The normalized electric field $\mathcal{E}(x(T), T)$ as seen by a particle in the field of 10 waves. The wave parameters are $\epsilon_i = 1$ m, $\nu_i = 3i$, $k_i = 1$ m^{-1} and $\varphi_i = 0$ for $i = 1, \ldots, 10$. The horizontal axis shows the number of spatial periods of the slowest wave, and integration parameter j is 20.

15. The normalized electric field $\mathcal{E}(x(T), T)$ as seen by a particle in the field of 10 waves. The wave parameters are $\epsilon_i = 1$ m, with ν_i, k_i and φ_i chosen at random for $i = 1, \ldots, 10$. The horizontal axis shows the number of spatial periods of the slowest wave, and integration parameter j is 20.

16. Surface of section of the Hamiltonian (4) for $N = 4$. The wave parameters are $\epsilon_i = 1.75$ m, $\nu_i = 5i$, $k_i = 0.7$ m^{-1} and $\varphi_i = 0$ for $i = 1, \ldots, 4$. Points are plotted at the times $T_p = 2\pi p/\nu_1$, for $p = 1, \ldots, 15000$. The initial gyroradius is 2.5 m, and the integration parameter $j = 17.5$ is not an integer in this special case.

17. Surface of section of the Hamiltonian (4) for $N = 5$. Wave parameters are $\epsilon_i = 1.8$ m, $(\nu_1, \ldots, \nu_5) = (5, 10, 10, 15, 15)$, $(k_1, \ldots, k_5) = (0.7, 0.75, 0.55, 0.7,$

0.35) m^{-1} and $\varphi_i = 0$ for $i = 1, \ldots, 5$. Points are plotted at the times $T_p = 2\pi p/\nu_1$, for $p = 1, \ldots, 15000$. The initial gyroradius is 2.6 m, and the integration parameter is $j = 22$.

18. Surface of section of the Hamiltonian (4) for $N = 6$. Wave parameters are $\epsilon_i = 1.8$ m, $(\nu_1, \ldots, \nu_6) = (5, 10, 10, 15, 15, 20)$, $(k_1, \ldots, k_6) = (0.7, 0.75, 0.55, 0.7, 0.35, 0.7)$ m^{-1} and $\varphi_i = 0$ for $i = 1, \ldots, 6$. Points are plotted at the times $T_p = 2\pi p/\nu_1$, for $p = 1, \ldots, 15000$. The initial gyroradius is 2.6 m, and the integration parameter $j = 17.5$ is not an integer in this special case.

19. Time-averaged ion distribution $N(\rho)$ versus gyroradius ρ for the Hamiltonian (4). Ten ions in the field of ten waves are averaged over the interval $200\pi \leq T \leq 2000\pi$. The wave parameters are chosen at random according to the prescriptions in the text (case A), with the mode amplitude range $[\epsilon_{min}, \epsilon_{max}] = [0, 1]$ m. The integration parameter j is 25.

20. Same as [19], except $[\epsilon_{min}, \epsilon_{max}] = [0.5, 1.5]$ m.

21. Same as [19], except $[\epsilon_{min}, \epsilon_{max}] = [1, 2]$ m.

22. Same as [19], except $[\epsilon_{min}, \epsilon_{max}] = [1.5, 2.5]$ m.

23. Same as [19], except $[\epsilon_{min}, \epsilon_{max}] = [2, 2.5]$ m.

24. Same as [19], except $[\epsilon_{min}, \epsilon_{max}] = [3, 3.5]$ m.

25. Time-averaged ion distribution $N(\rho)$ versus gyroradius ρ for the Hamiltonian (4). Ten ions in the field of ten waves are averaged over the interval $200\pi \leq T \leq 2000\pi$. The wave parameters are chosen at random according to the prescriptions in the text (case B), with the mode amplitude range $[\epsilon_{min}, \epsilon_{max}] = [0, 1]$ m. The integration parameter j is 25.

26. Same as [25], except $[\epsilon_{min}, \epsilon_{max}] = [0.5, 1.5]$ m.

27. Same as [25], except $[\epsilon_{min}, \epsilon_{max}] = [1, 2]$ m.

28. Same as [25], except $[\epsilon_{min}, \epsilon_{max}] = [1.5, 2.5]$ m.

29. Same as [25], except $[\epsilon_{min}, \epsilon_{max}] = [2, 2.5]$ m.

30. Same as [25], except $[\epsilon_{min}, \epsilon_{max}] = [3, 3.5]$ m.

31. Qualitative particle trajectory in the $(\dot{x}, \dot{y})$ phase plane for the Hamiltonian (2). In the oval regions, a resonant interaction occurs which may lead to a substantial phase change and thus to stochastic particle dynamics. This effect weakens as the gyroradius of a particular trajectory increases.

Table I: Summary of Turbulent Spectrum Heating Simulations.

Run	Wave Parameters	$\epsilon_{min} - \epsilon_{max}$ (m)	ρ_{max} (m)	$\mathcal{T}_{max}$ (eV)
1A	$\left\{\nu_i^{(A)}, k_i^{(A)}, \varphi_i^{(A)}\right\}_{i=1}^{10}$	$0 - 1$	14	1.5×10^1
2A		$0.5 - 1.5$	29	6.4×10^1
3A		$1 - 2$	51	2.0×10^2
4A		$1.5 - 2.5$	80	4.9×10^2
5A		$2 - 2.5$	83	5.3×10^2
6A		$3 - 3.5$	133	1.4×10^3
1B	$\left\{\nu_i^{(B)}, k_i^{(B)}, \varphi_i^{(B)}\right\}_{i=1}^{10}$	$0 - 1$	4	1.2×10^0
2B		$0.5 - 1.5$	5	1.9×10^0
3B		$1 - 2$	6	2.8×10^0
4B		$1.5 - 2.5$	60	2.8×10^2
5B		$2 - 2.5$	84	5.4×10^2
6B		$3 - 3.5$	108	8.9×10^2

Surface of Section

x(t)

p(t)
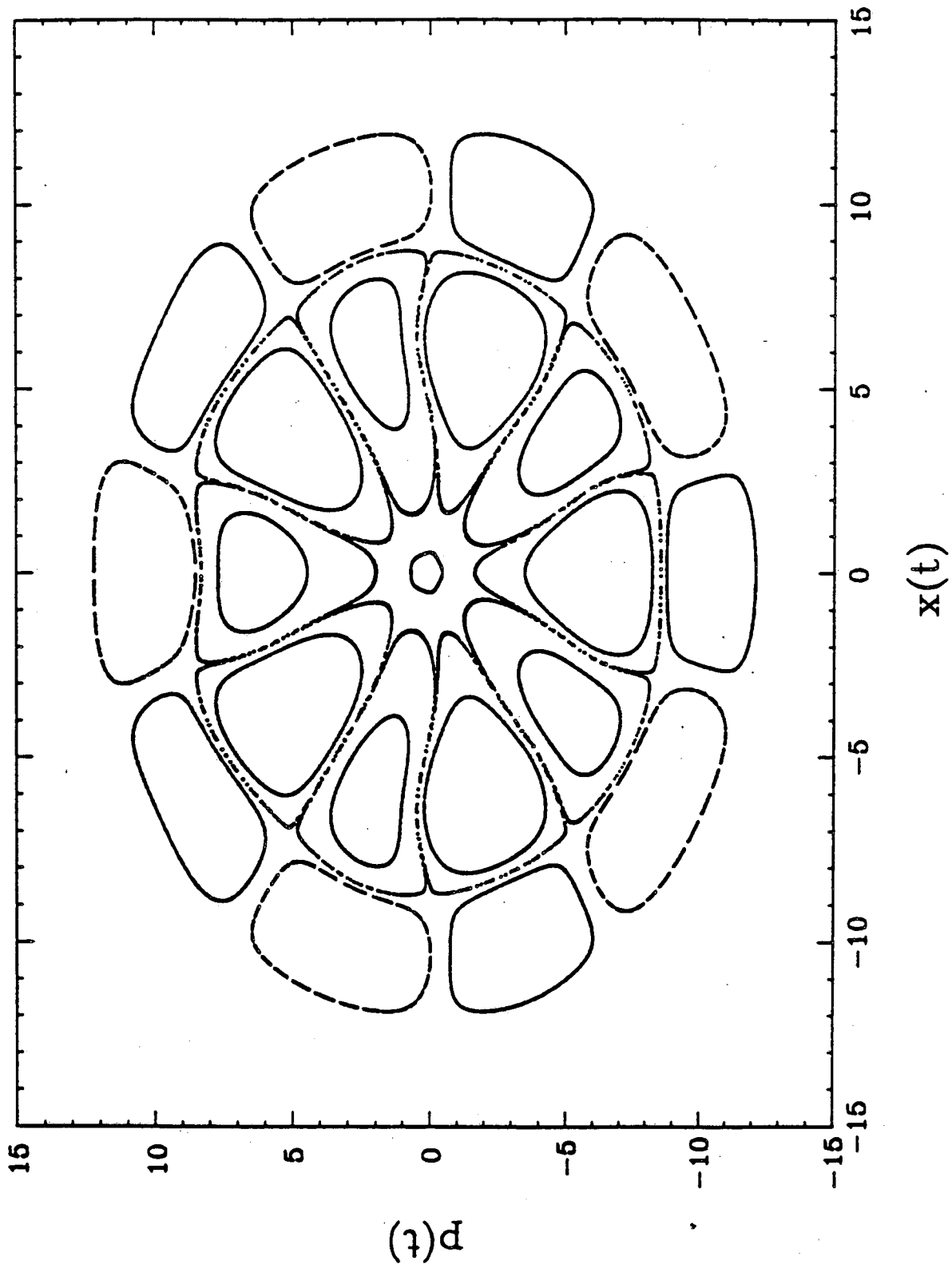
Fig. 1

Surface of Section

x(t)
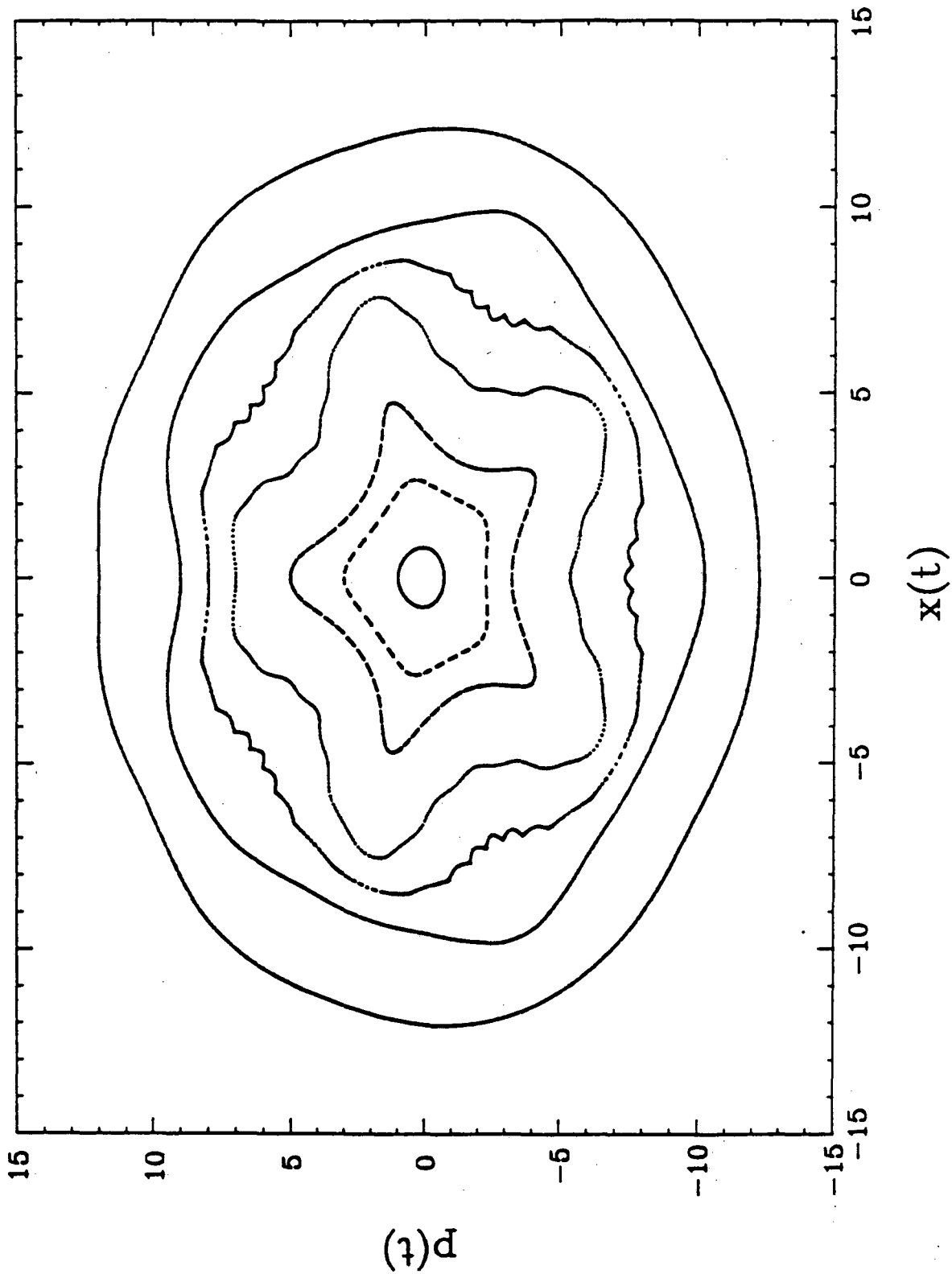
Fig. 2

Surface of Section

$x(t)$

$p(t)$

Fig. 3

28
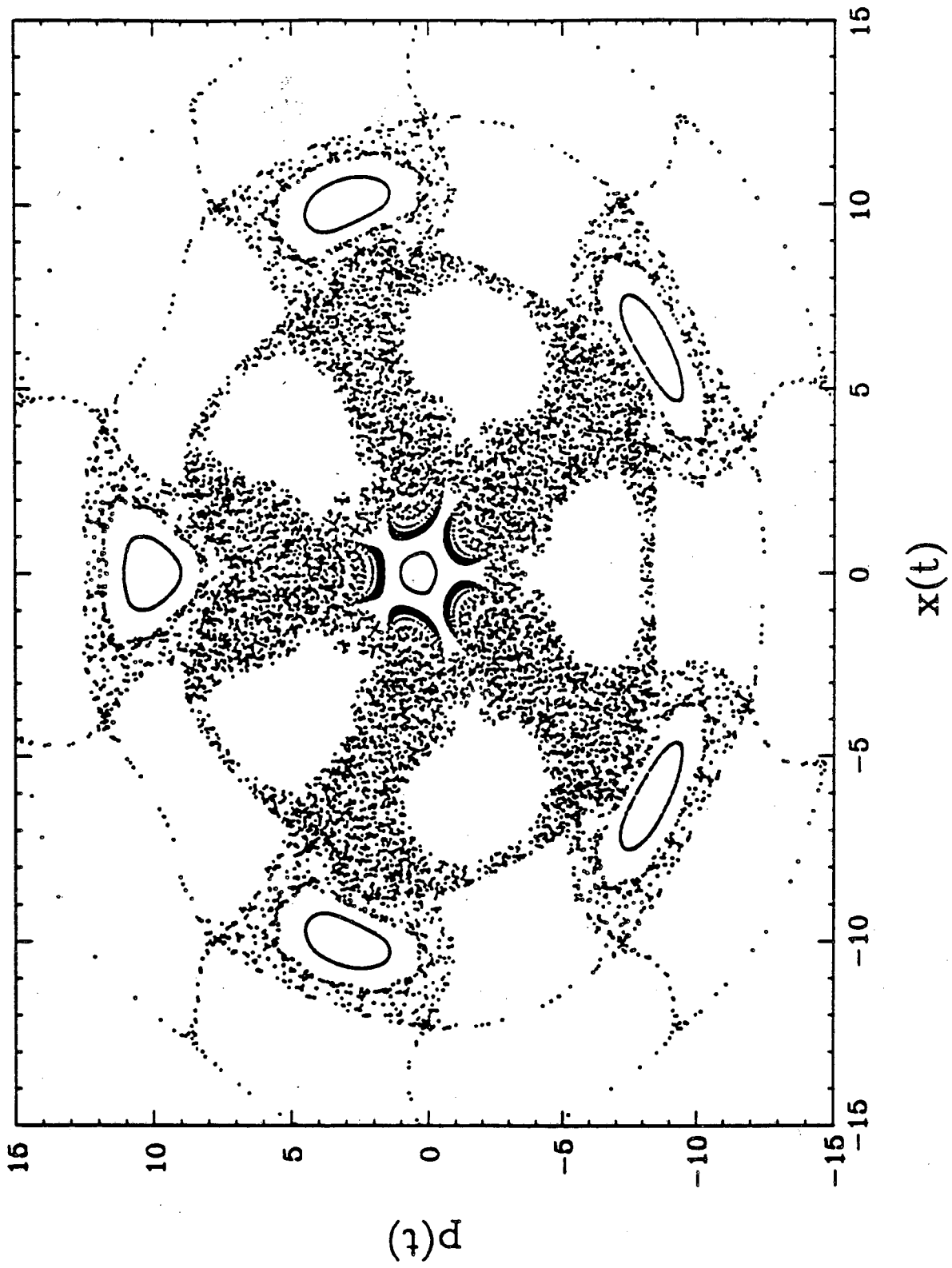
Surface of Section
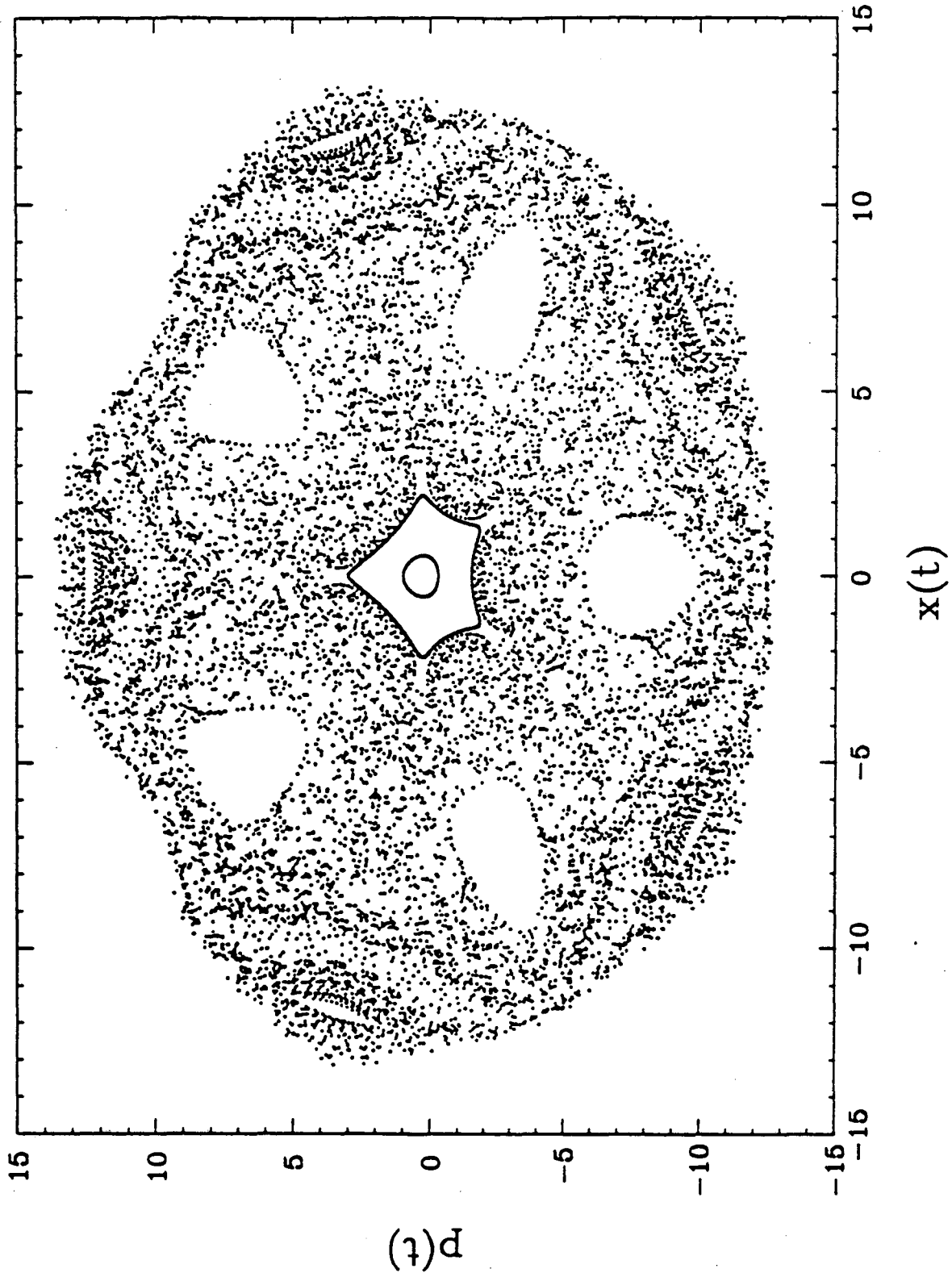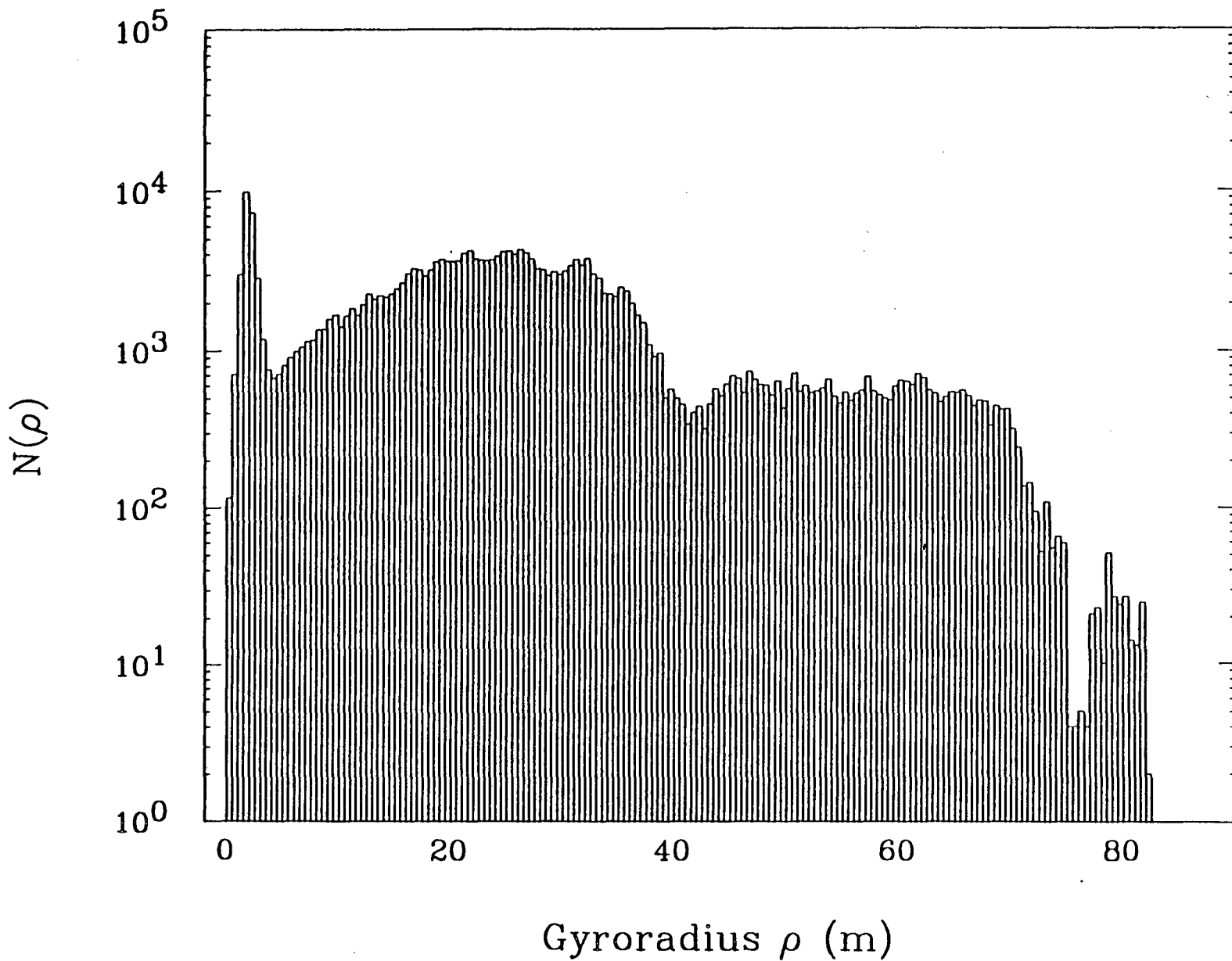

Fig. 4

Time-Averaged Ion Distribution
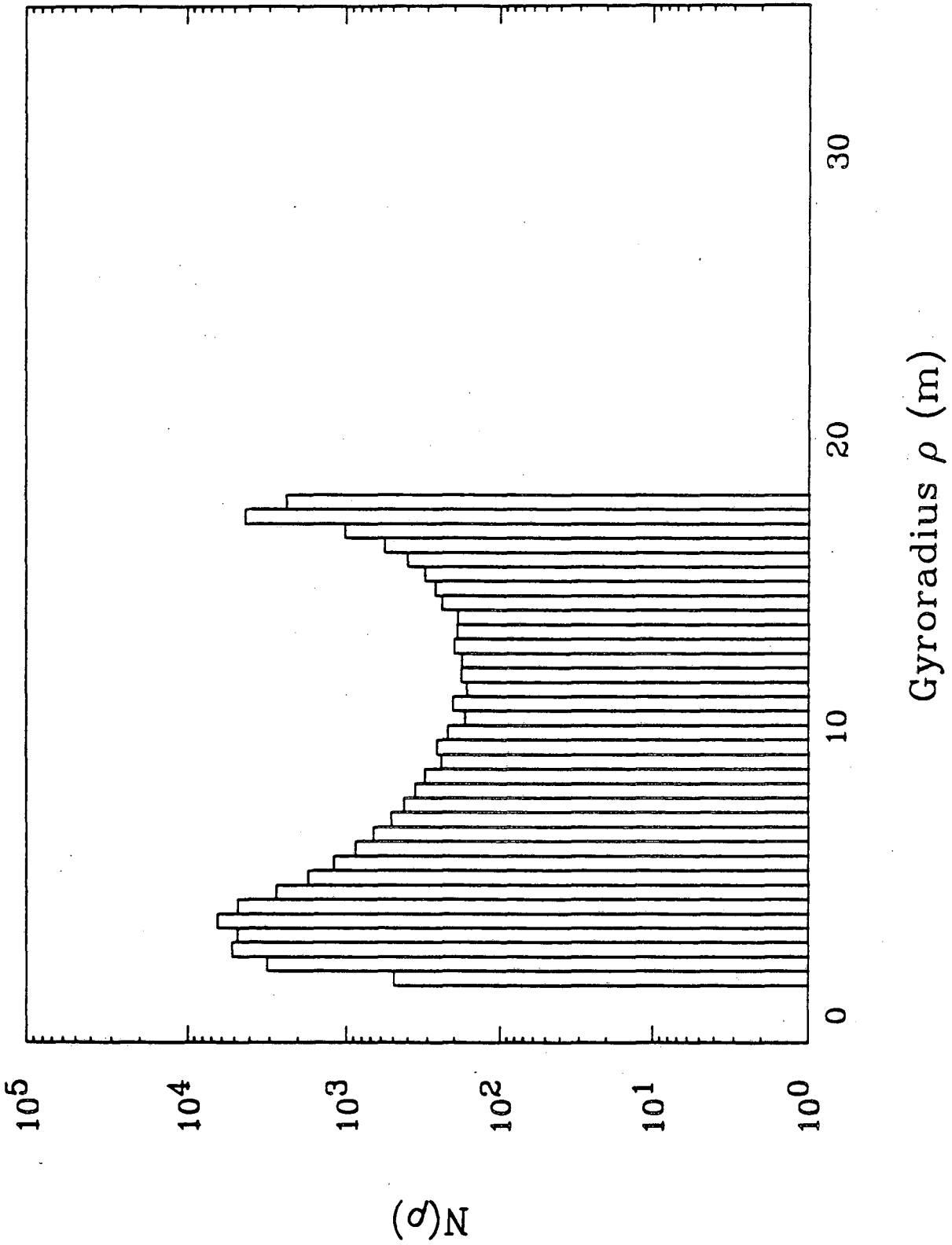
Fig. 5

Time–Averaged Ion Distribution

$N(\rho)$

Gyroradius ρ (m)

Fig. 6

31

Time−Averaged Ion Distribution

$N(\rho)$

Gyroradius ρ (m)
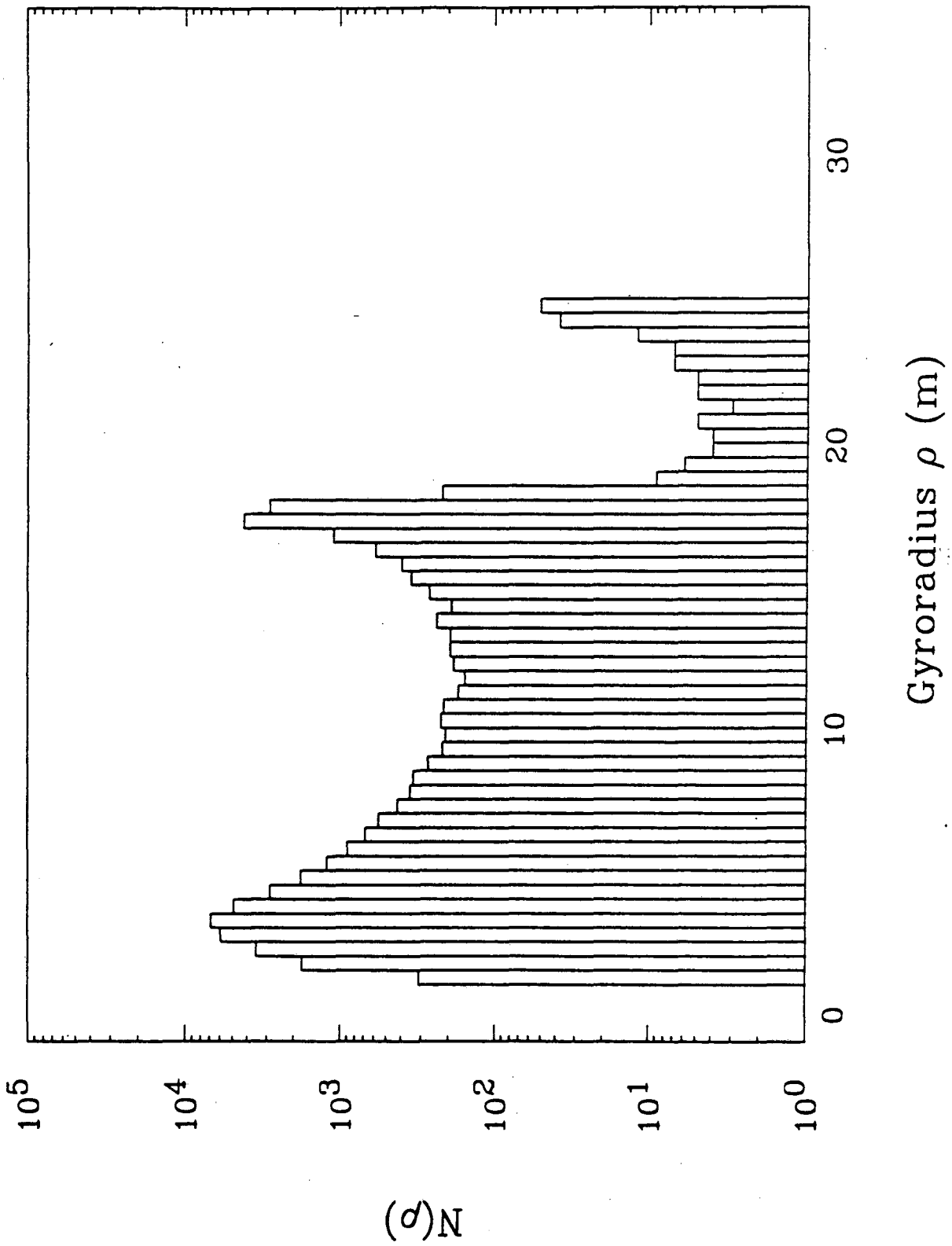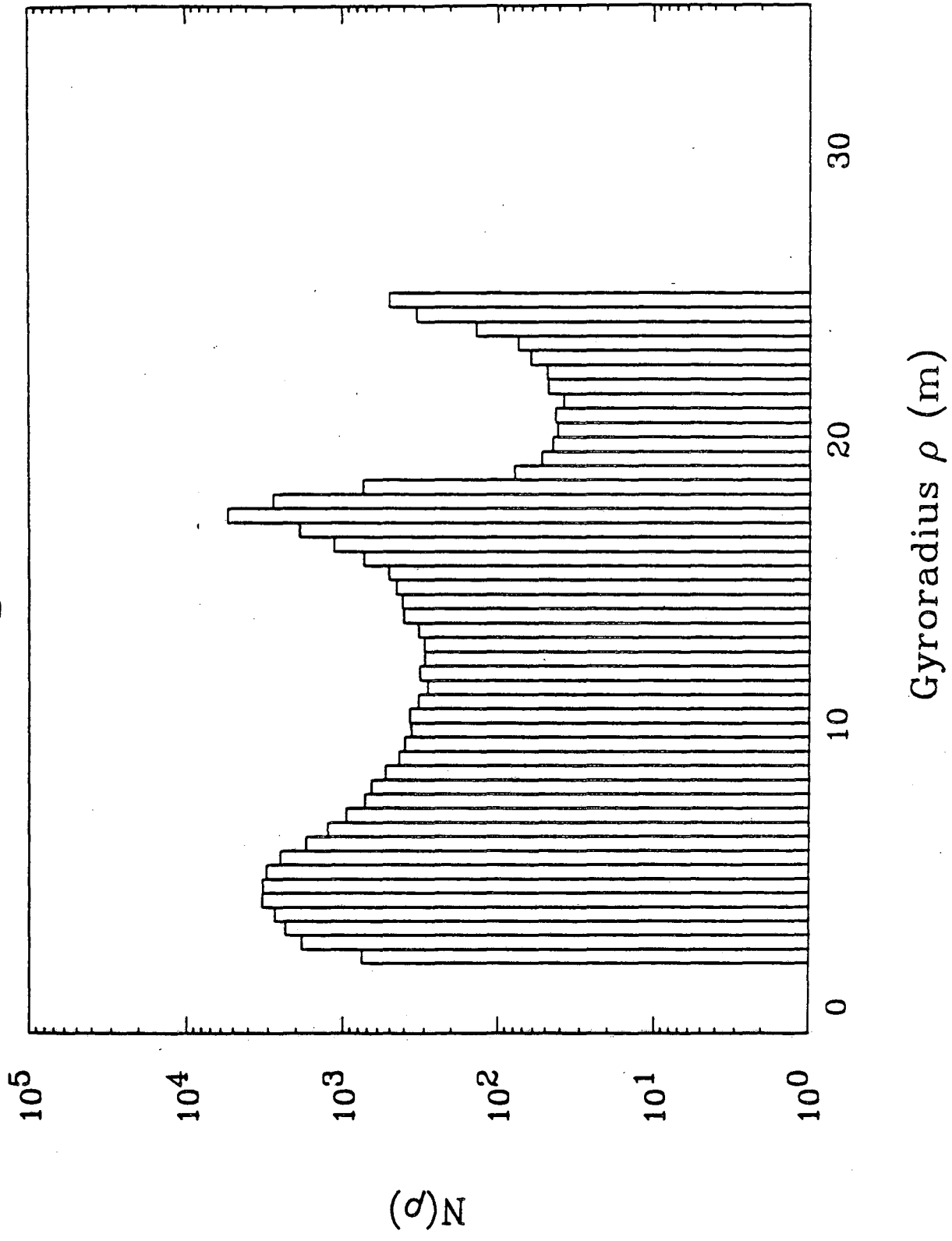
Fig. 7

Time−Averaged Ion Distribution

$N(\rho)$
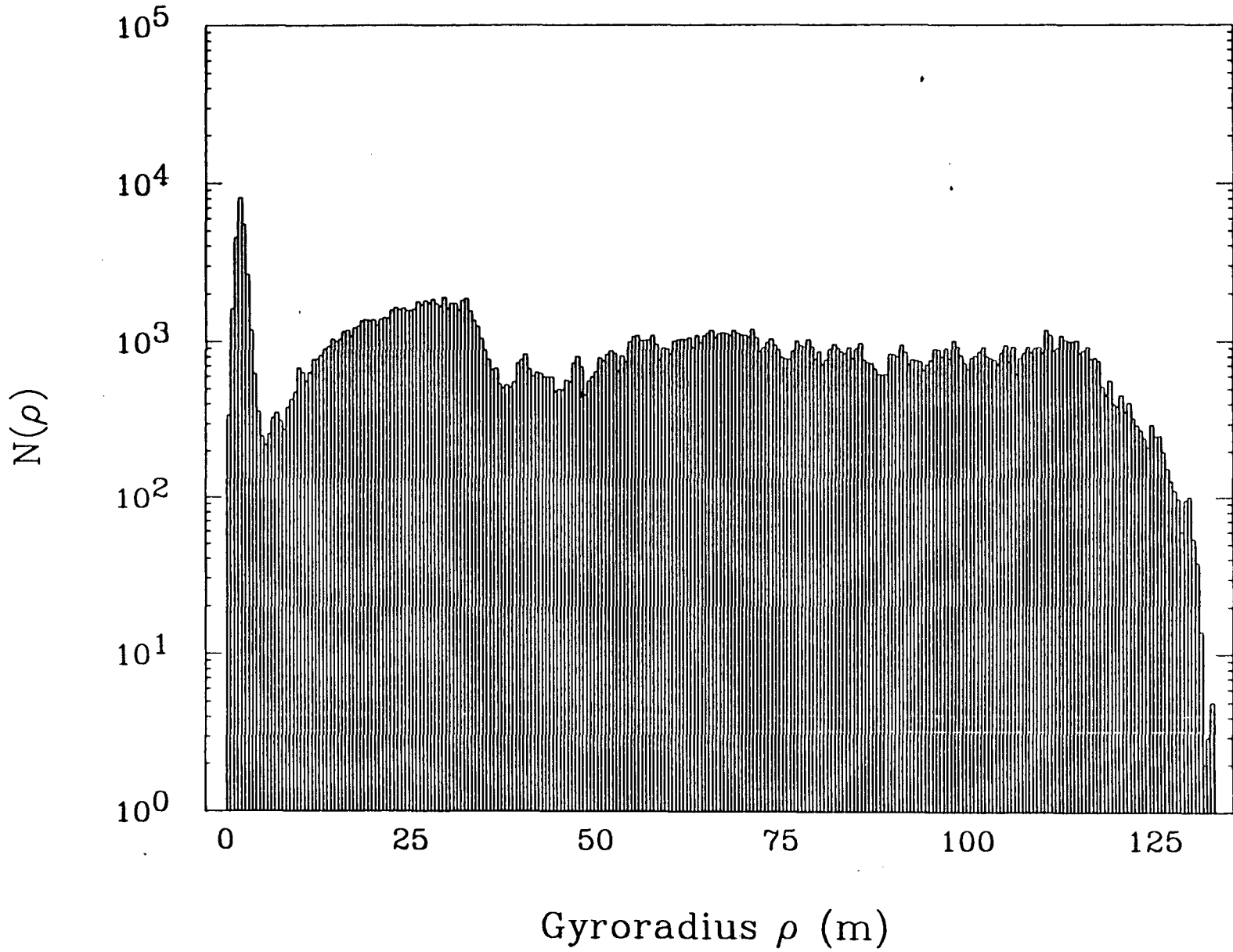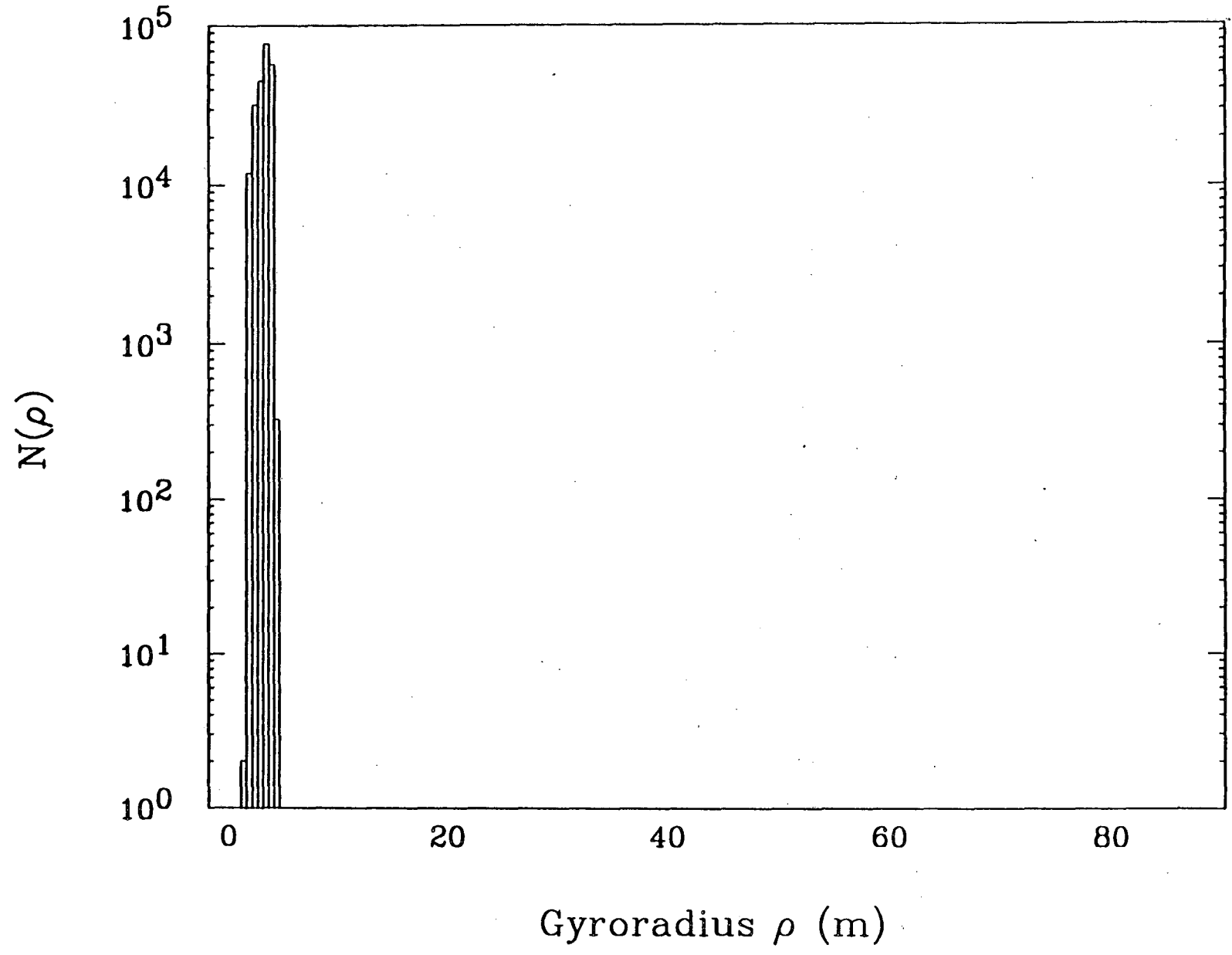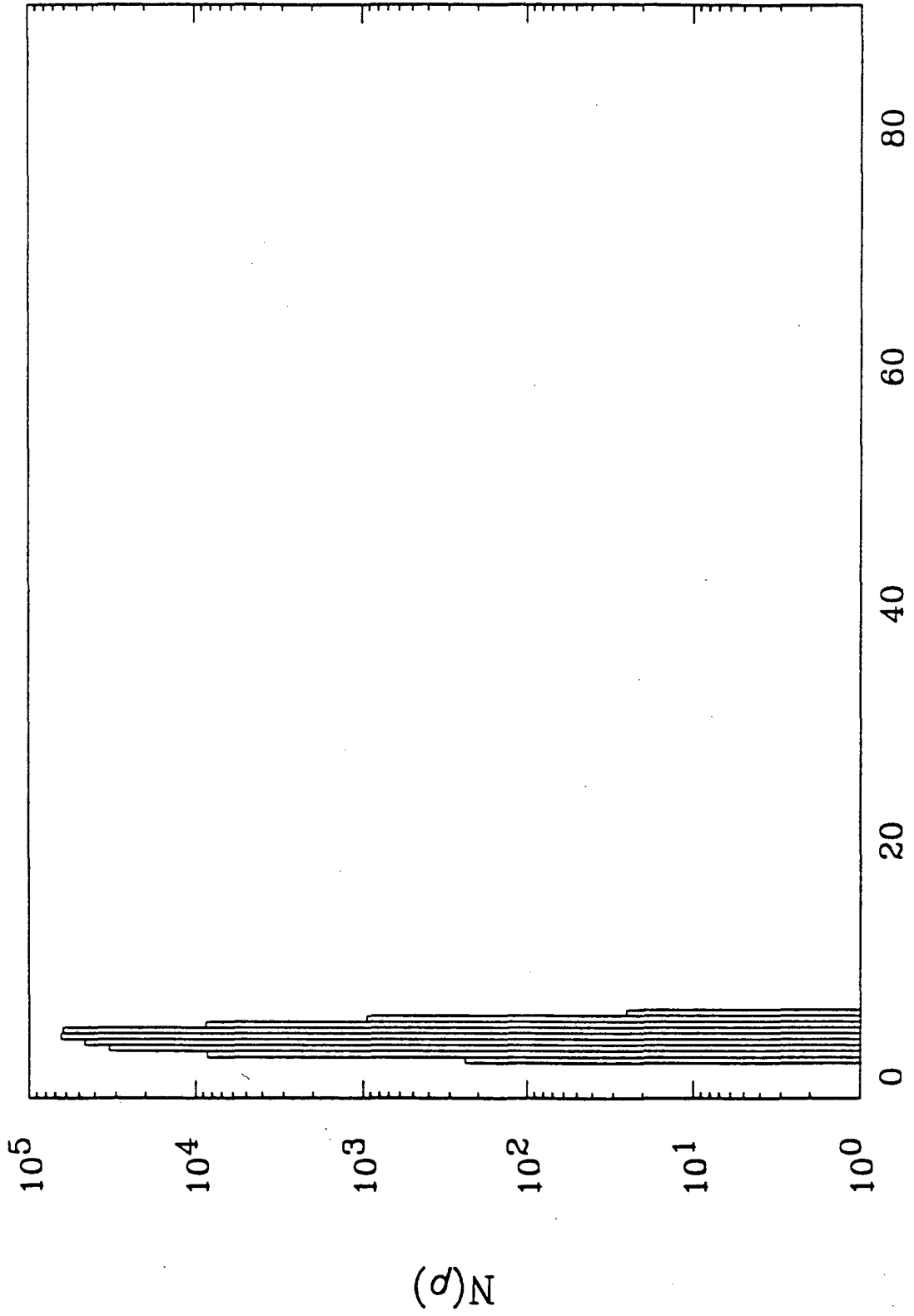
Gyroradius ρ (m)

Fig. 8

33
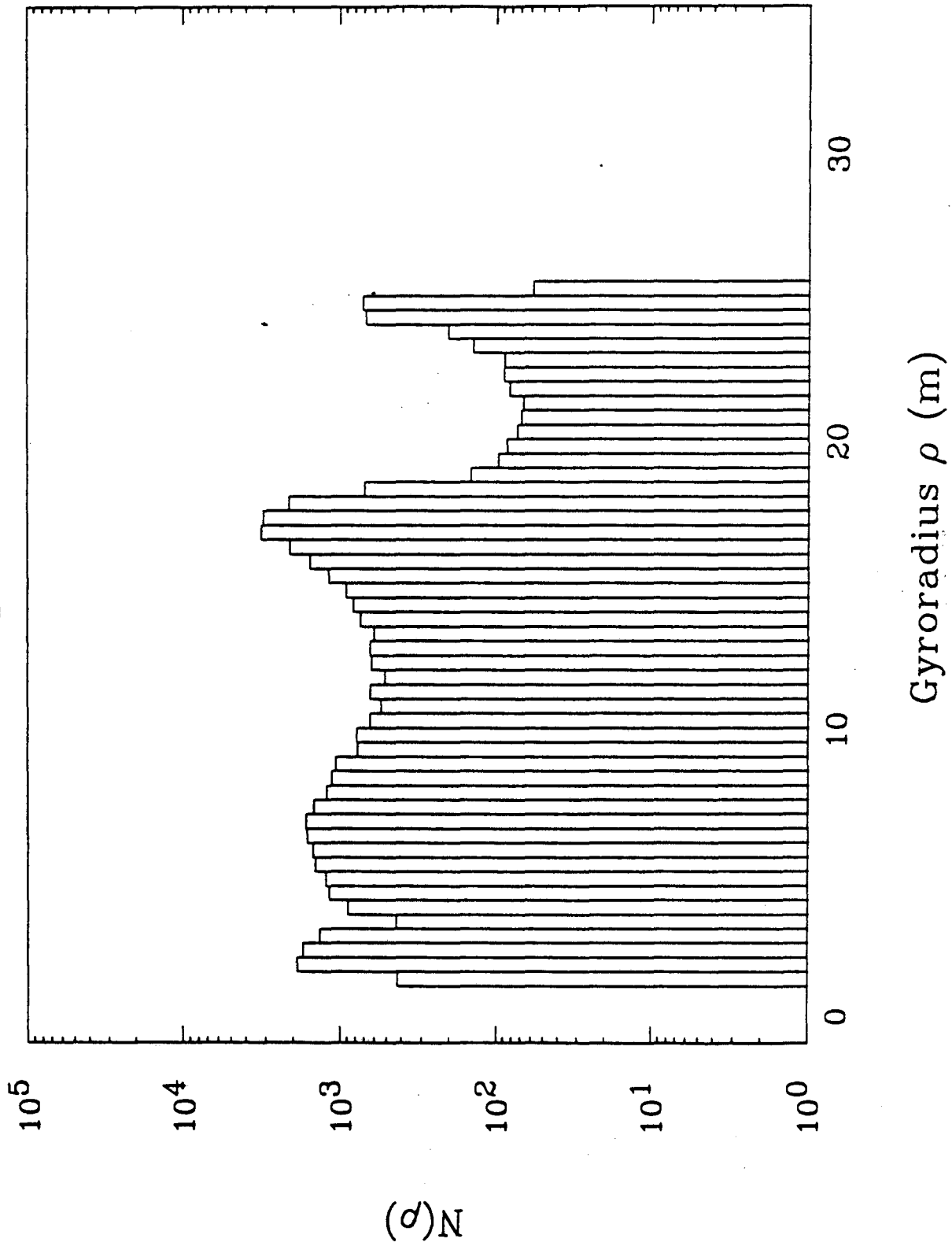
Time-Averaged Ion Distribution
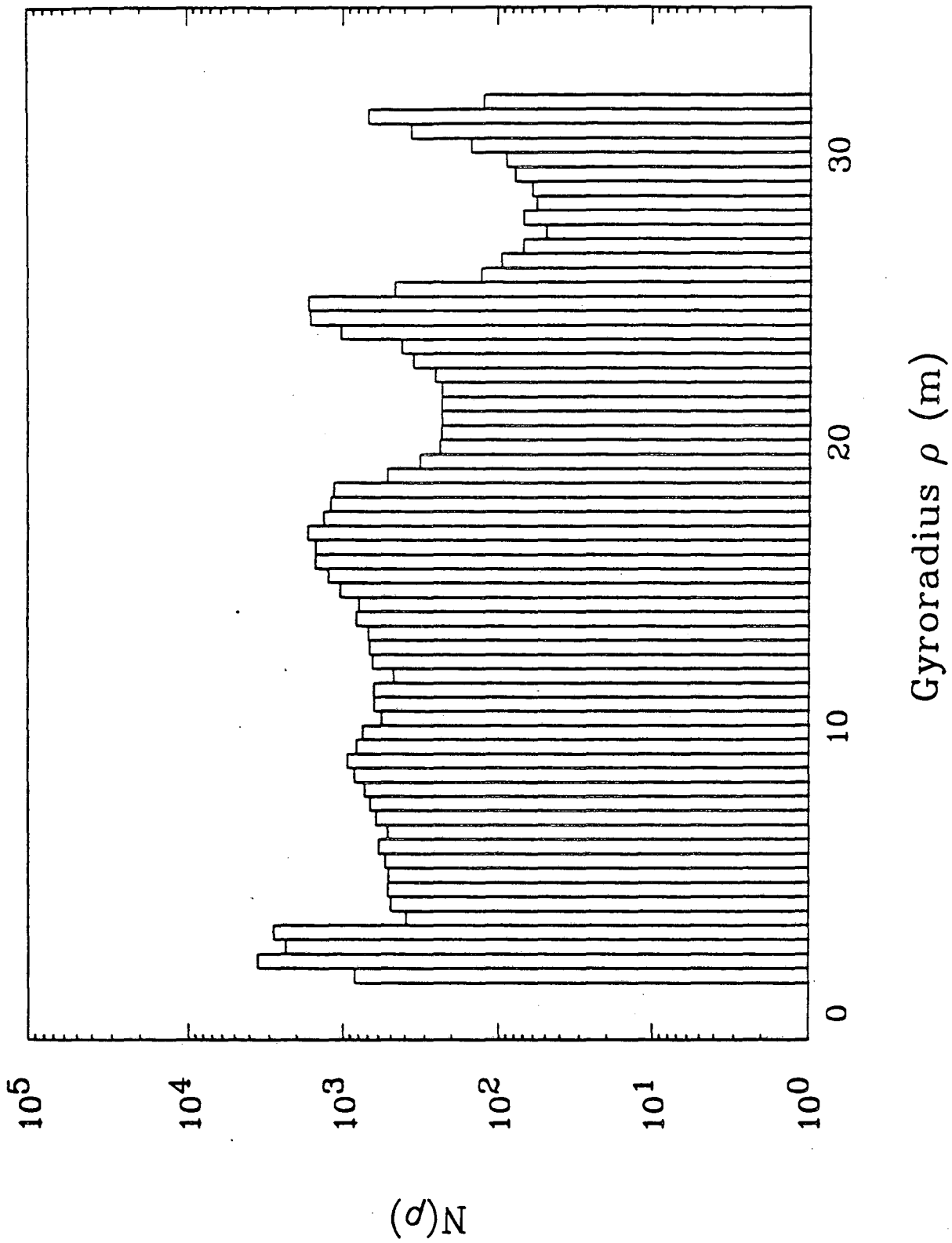
Fig. 9

Time-Averaged Ion Distribution

Gyroradius ρ (m)

$N(\rho)$
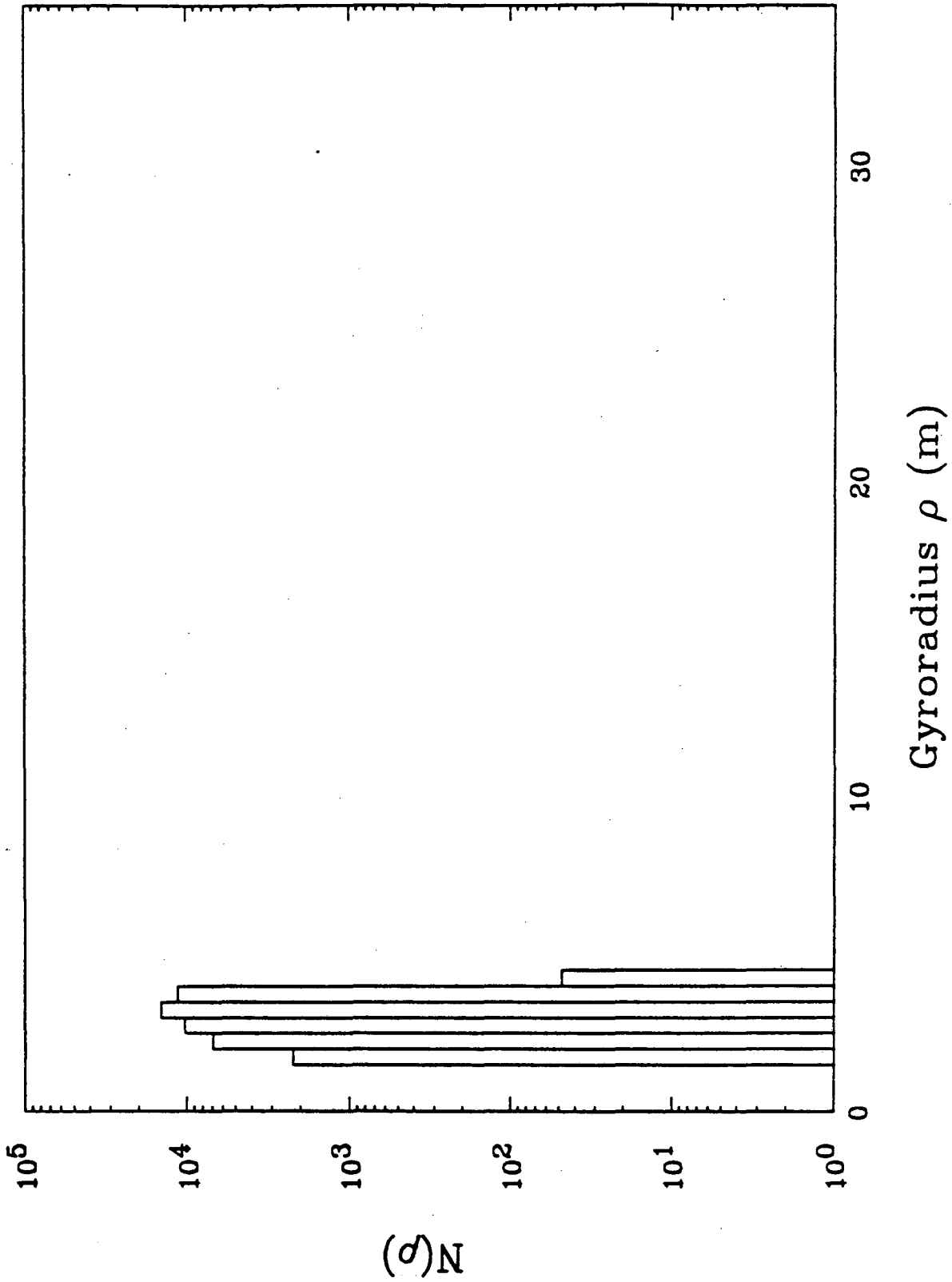
Fig. 10

Time-Averaged Ion Distribution

$N(\rho)$

Gyroradius ρ (m)
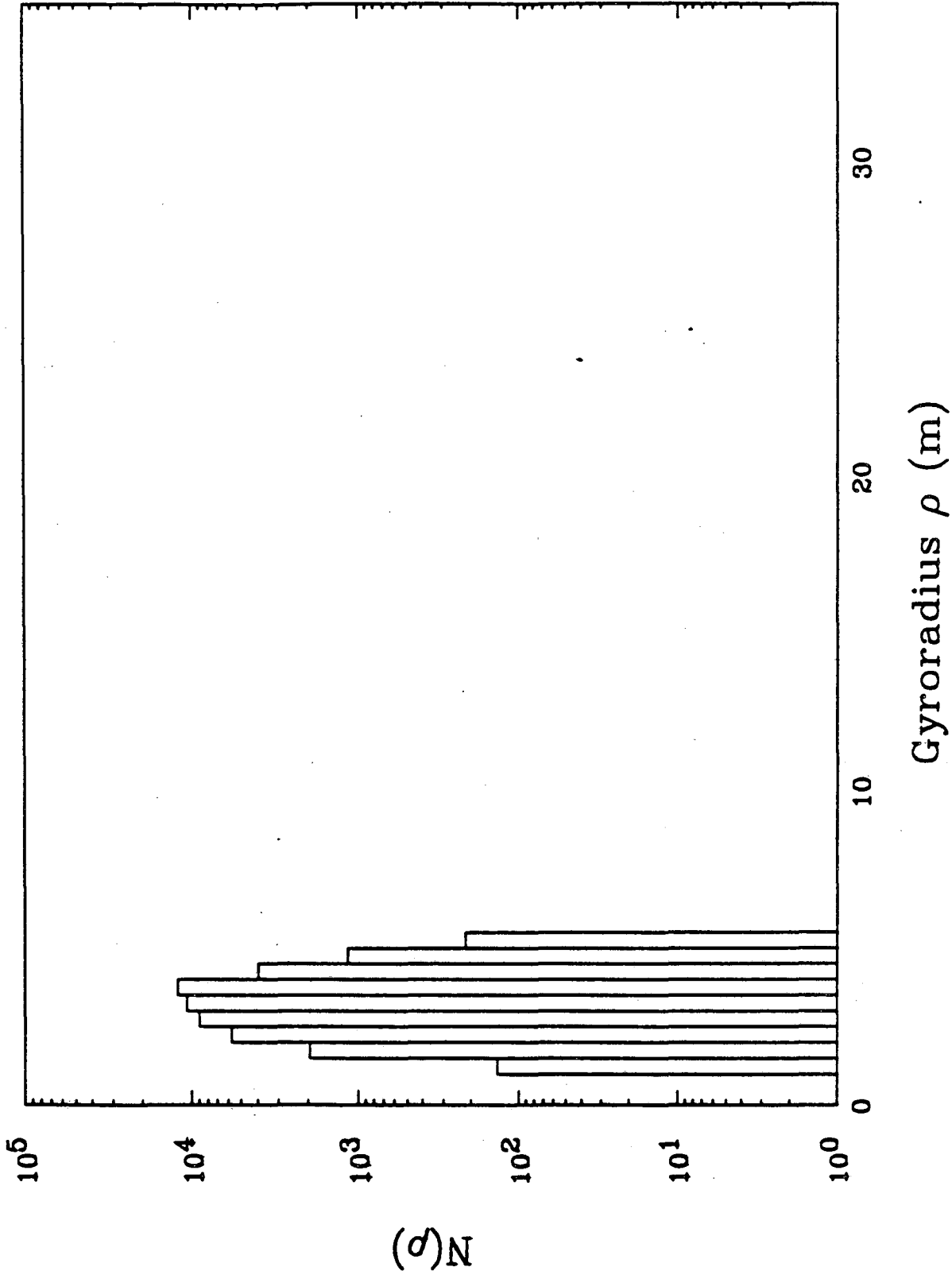
Fig. 11

Time–Averaged Ion Distribution

$N(\rho)$

Gyroradius ρ (m)

Fig. 12

37
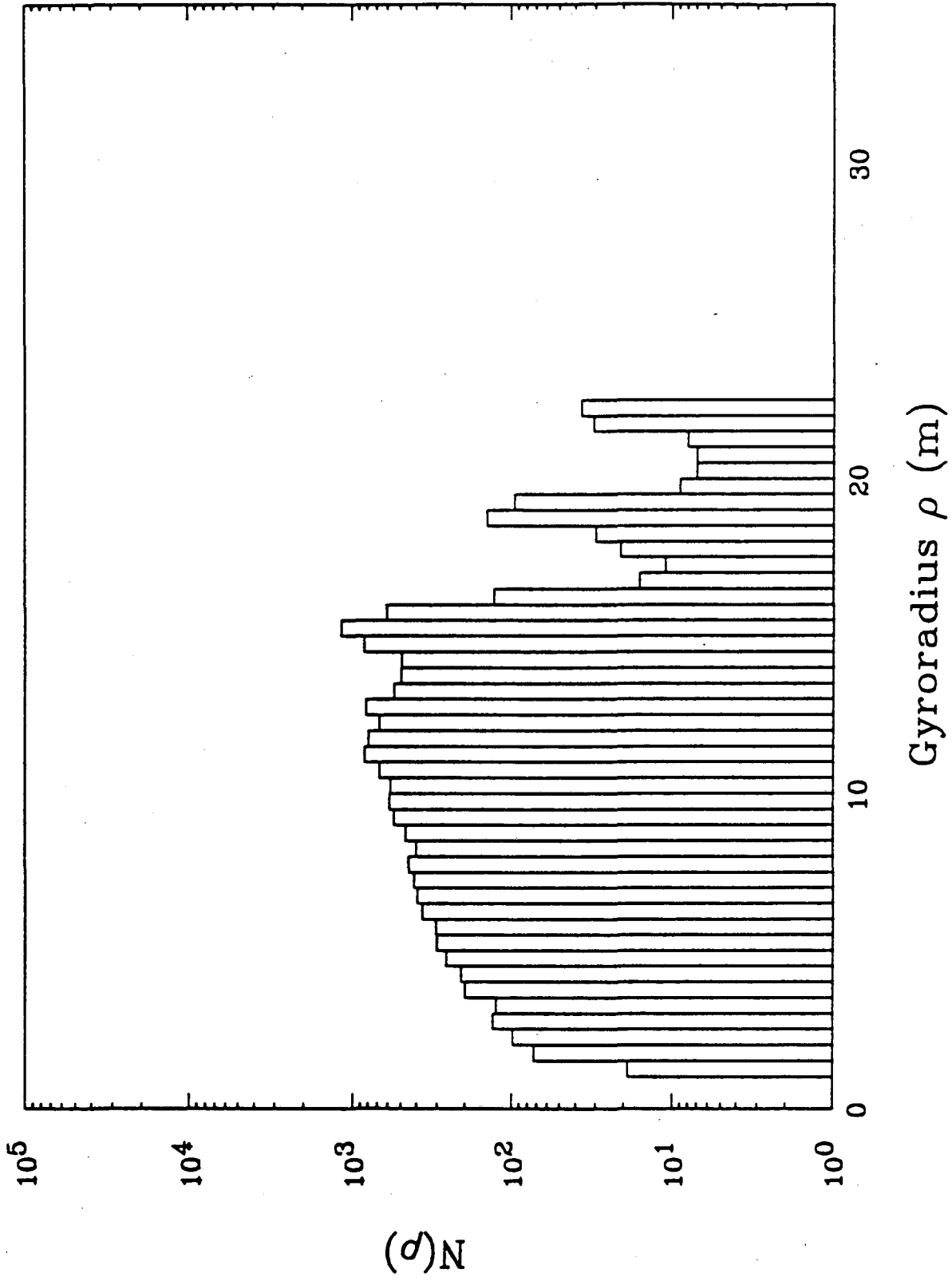
Time–Averaged Ion Distribution
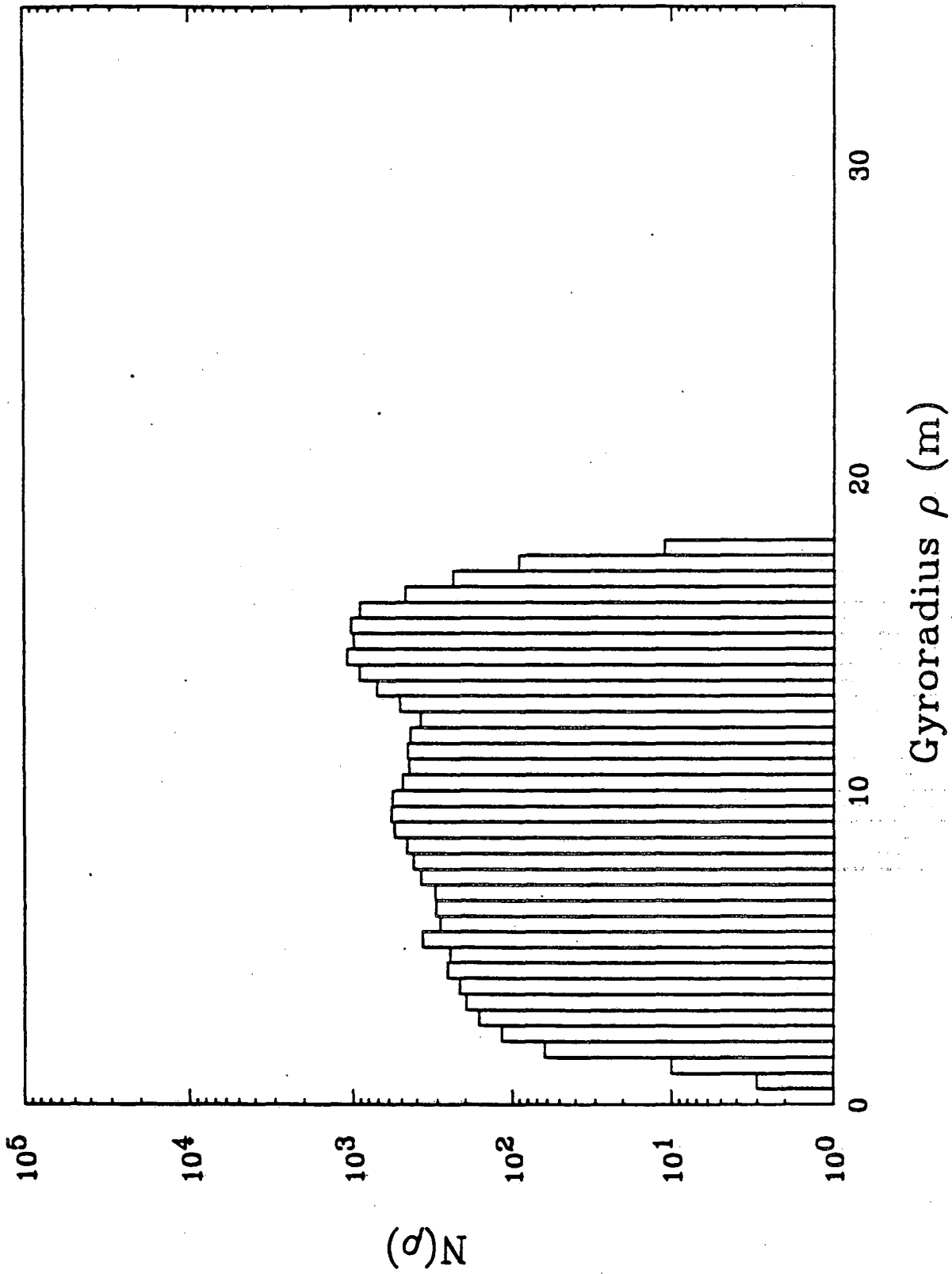
Fig. 13

Electric Field Amplitude
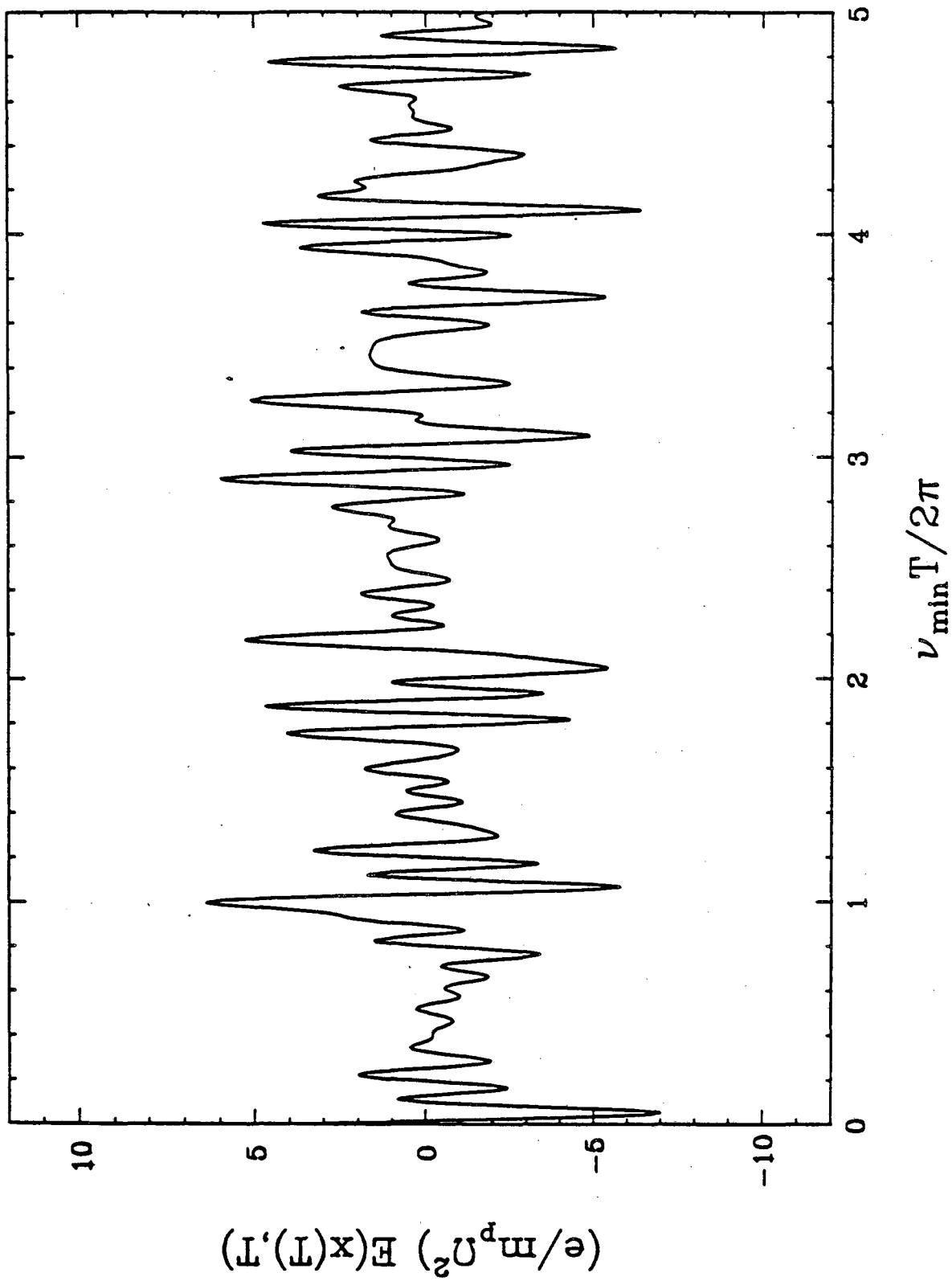
$\nu_{min}T/2\pi$

Fig. 14

$(e/m_p\Omega^2)\ \mathbb{E}(x(T),T)$

39

Electric Field Amplitude

Fig. 15

Surface of Section
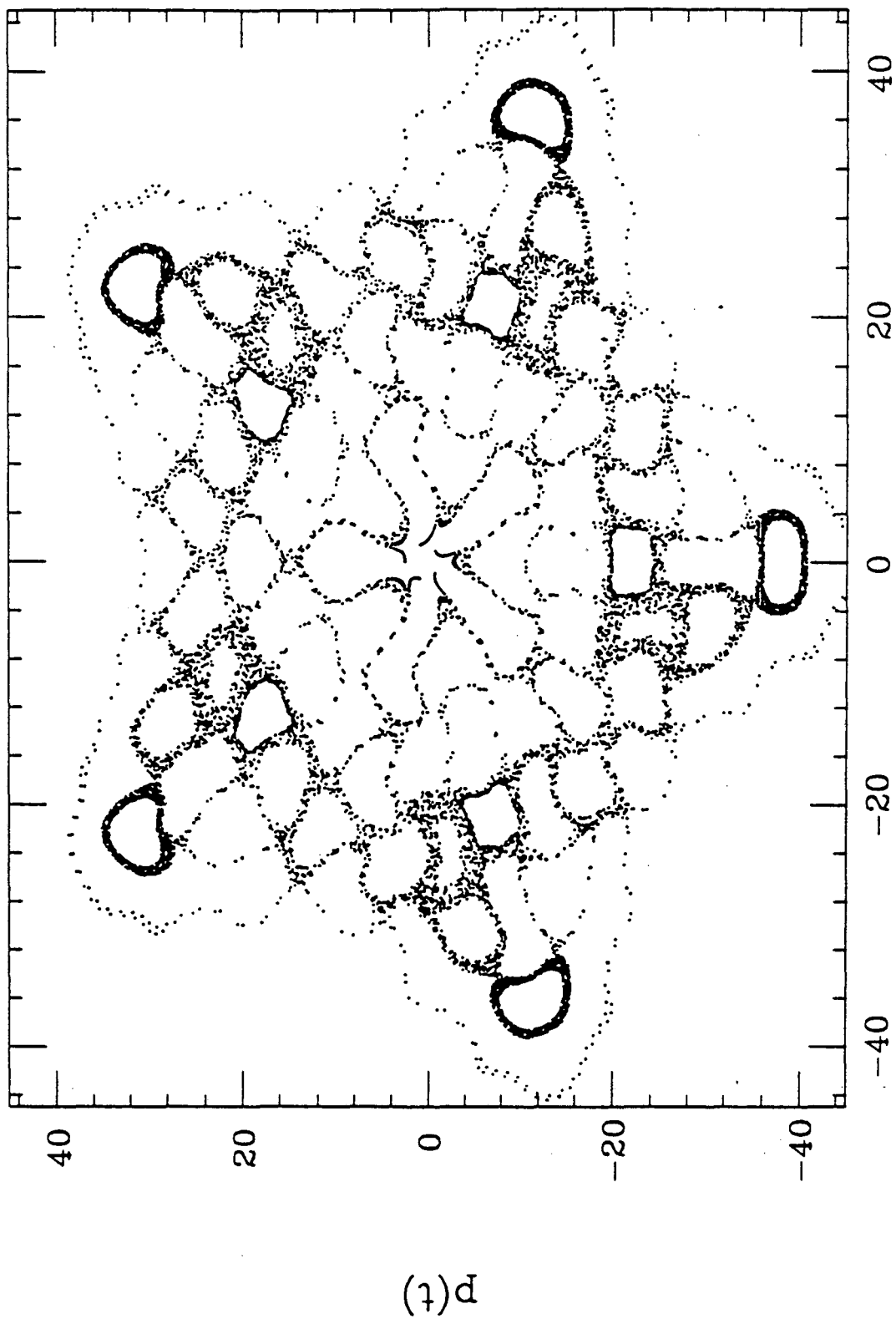
Fig. 16

41

Surface of Section

x(t)

Fig. 17

p(t)

Surface of Section

x(t)

p(t)

Fig. 18

43

Time−Averaged Ion Distribution

Gyroradius ρ (m)
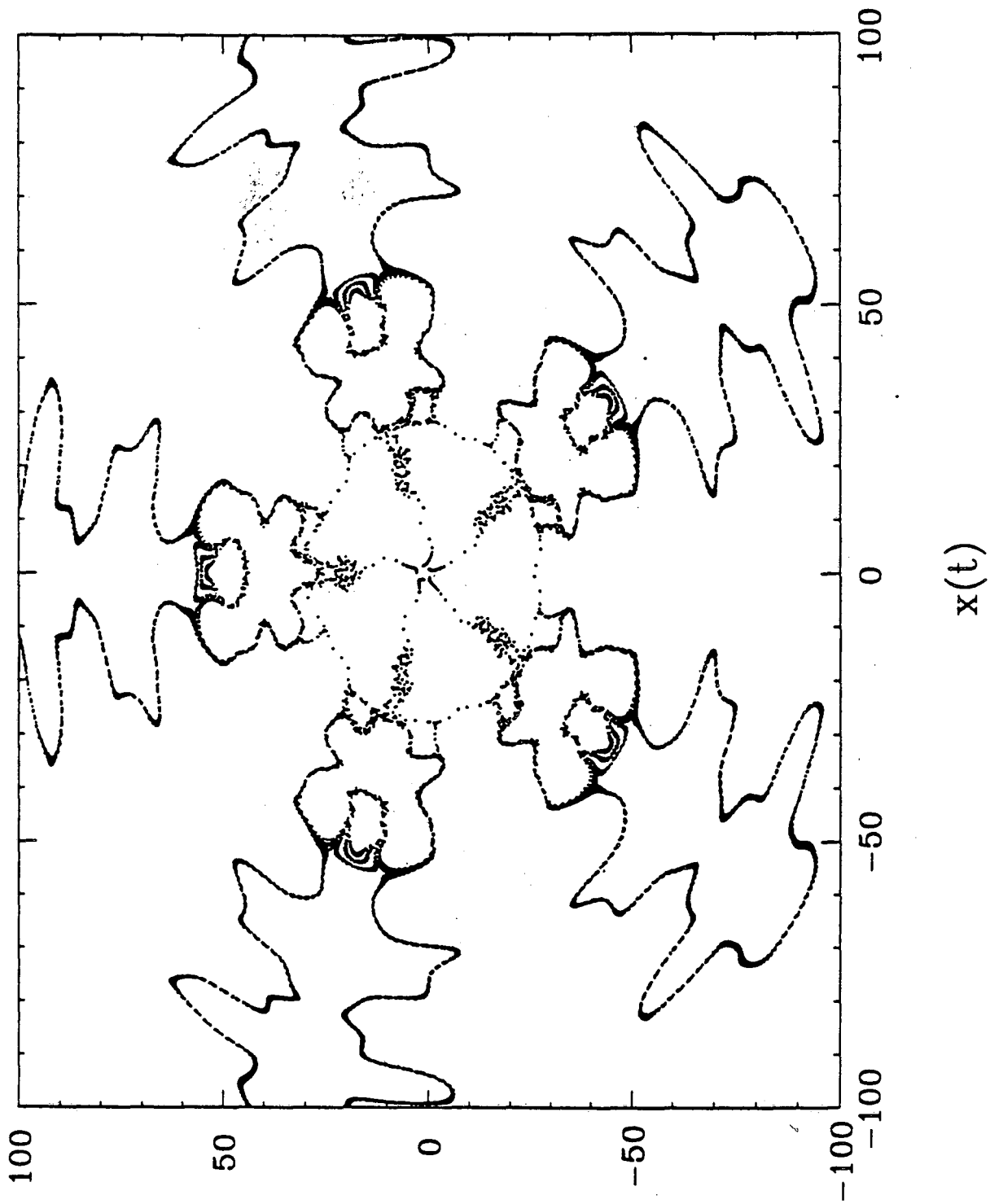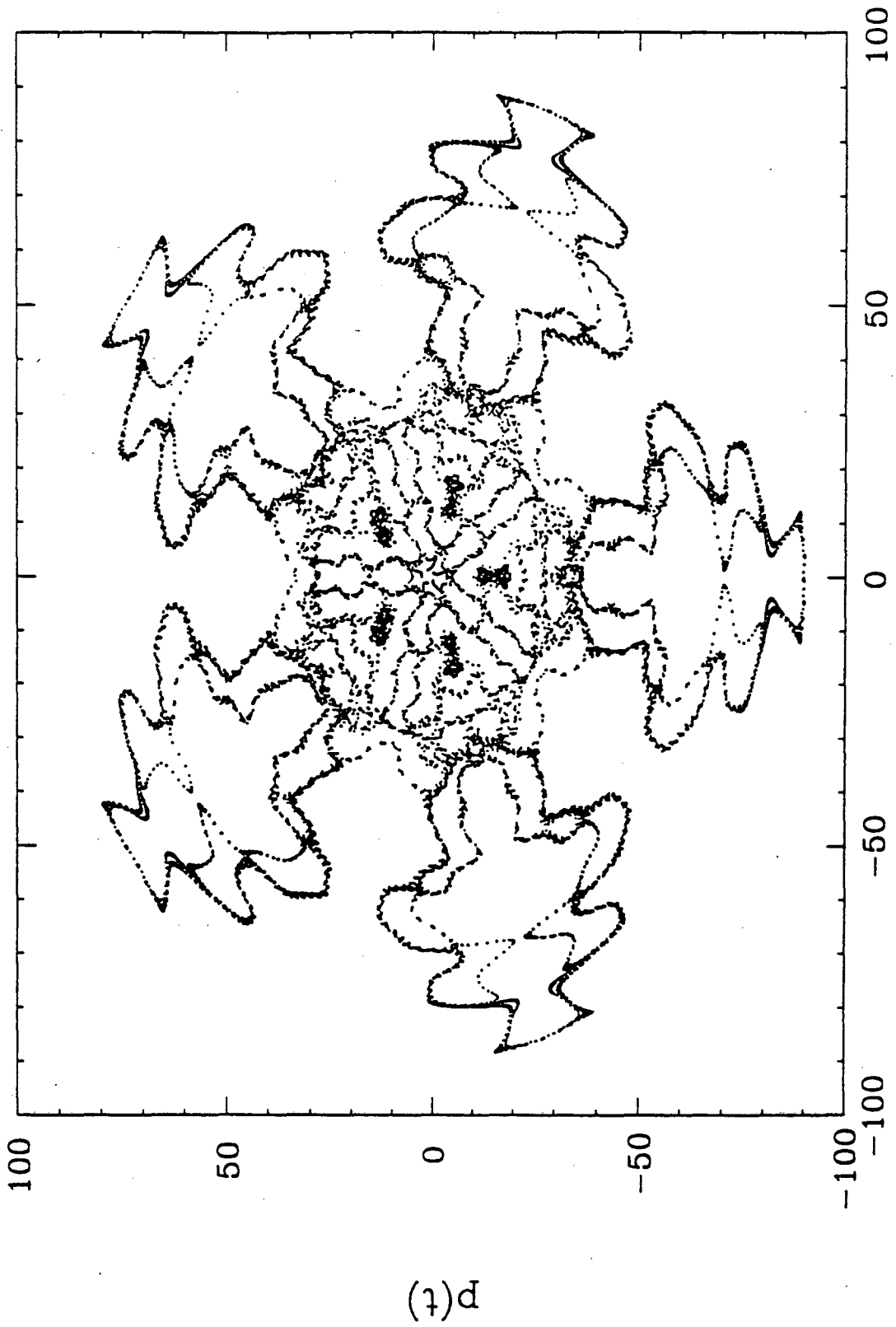
$N(\rho)$
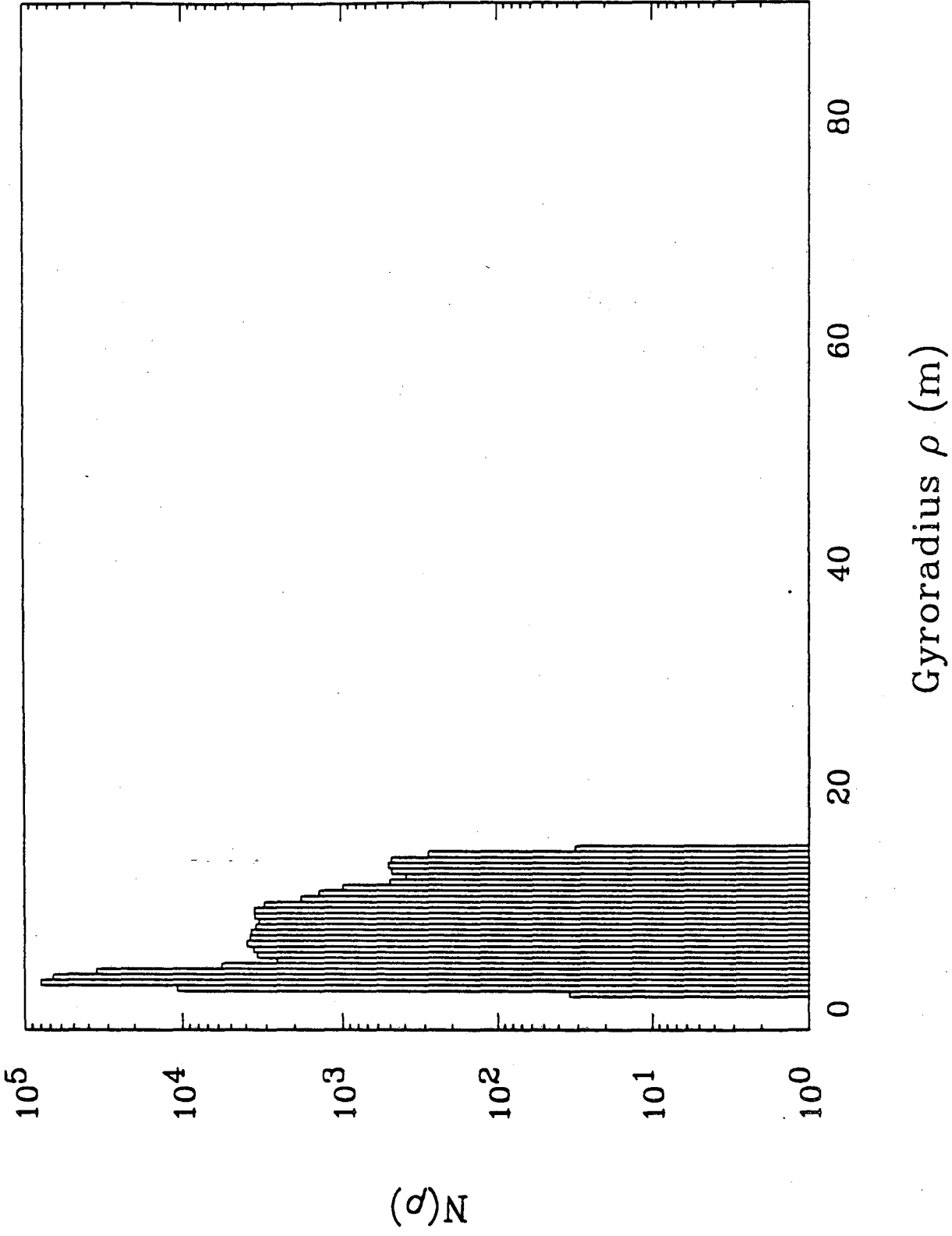
Fig. 19

Time—Averaged Ion Distribution

$N(\rho)$

Gyroradius ρ (m)
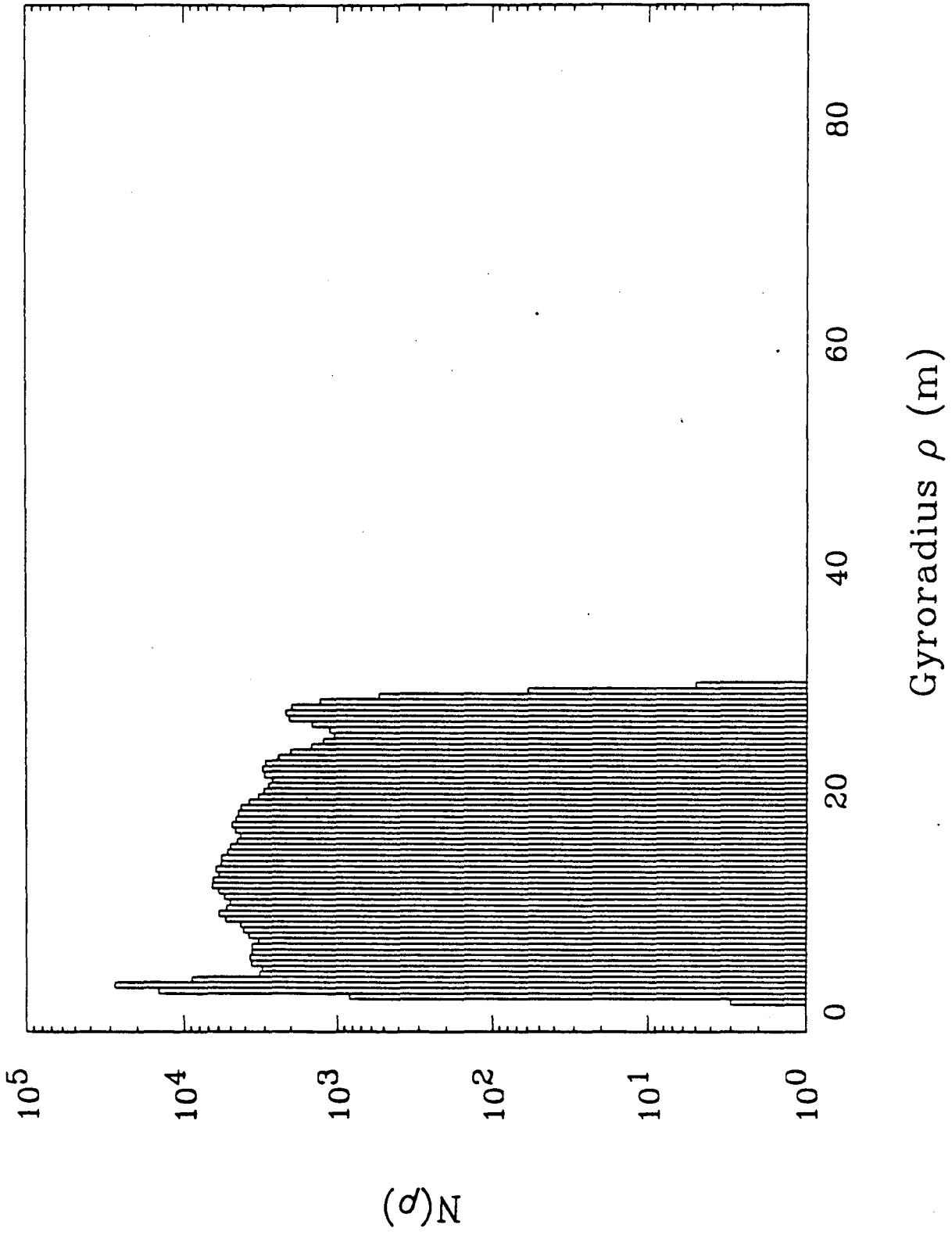
Fig. 20

Time–Averaged Ion Distribution
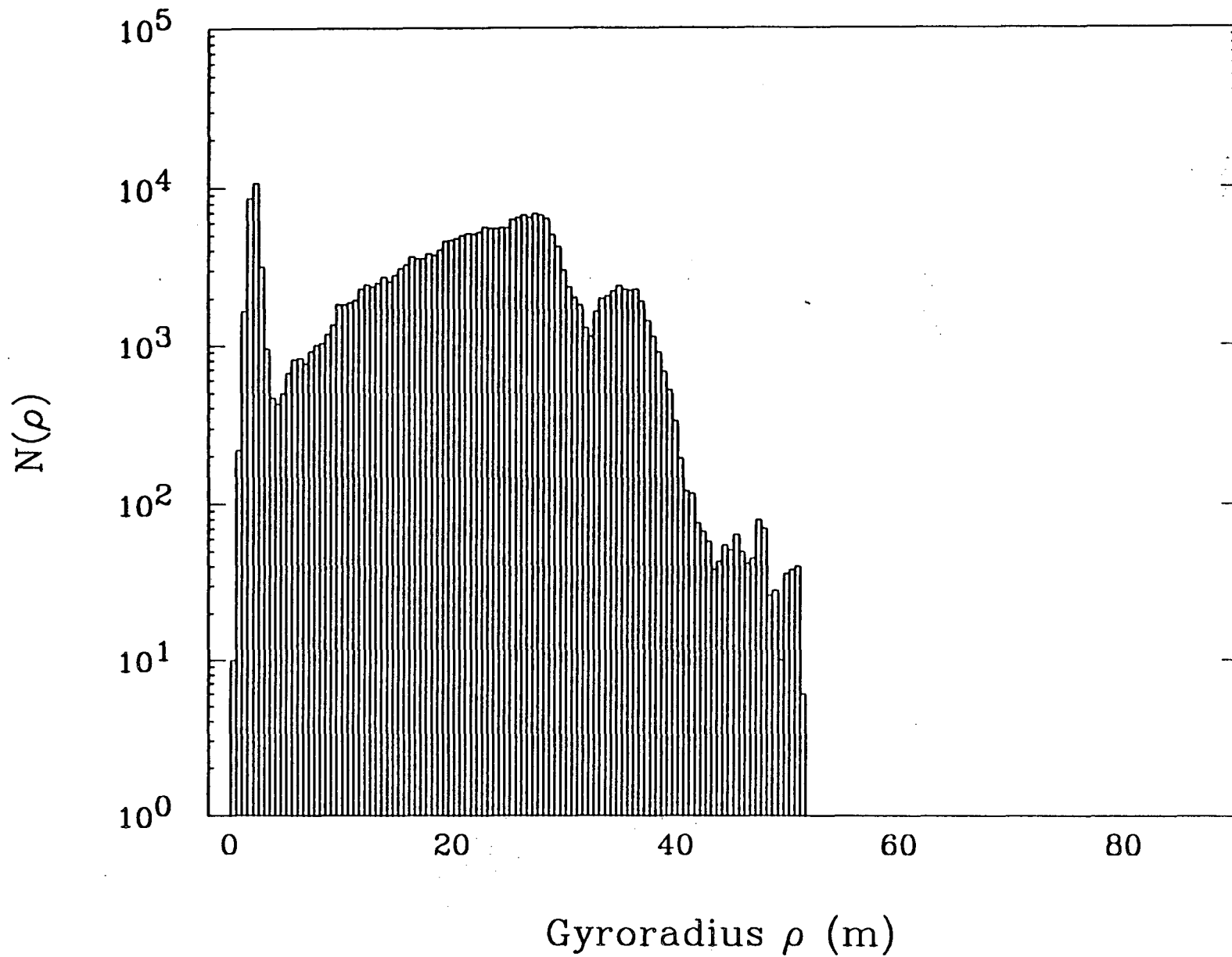
Gyroradius ρ (m)

Fig. 21

Time−Averaged Ion Distribution
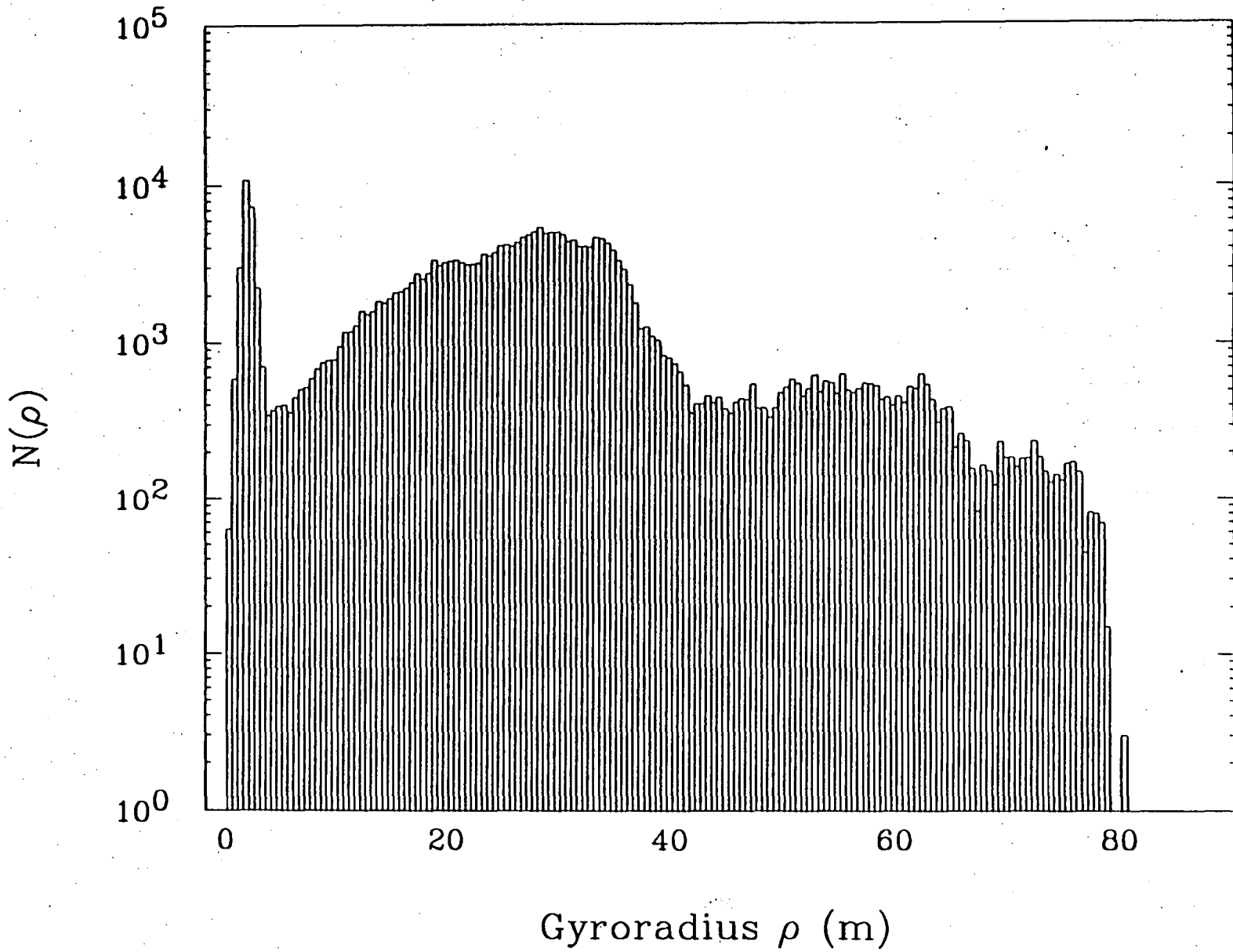
Gyroradius ρ (m)

Fig. 22

Time−Averaged Ion Distribution
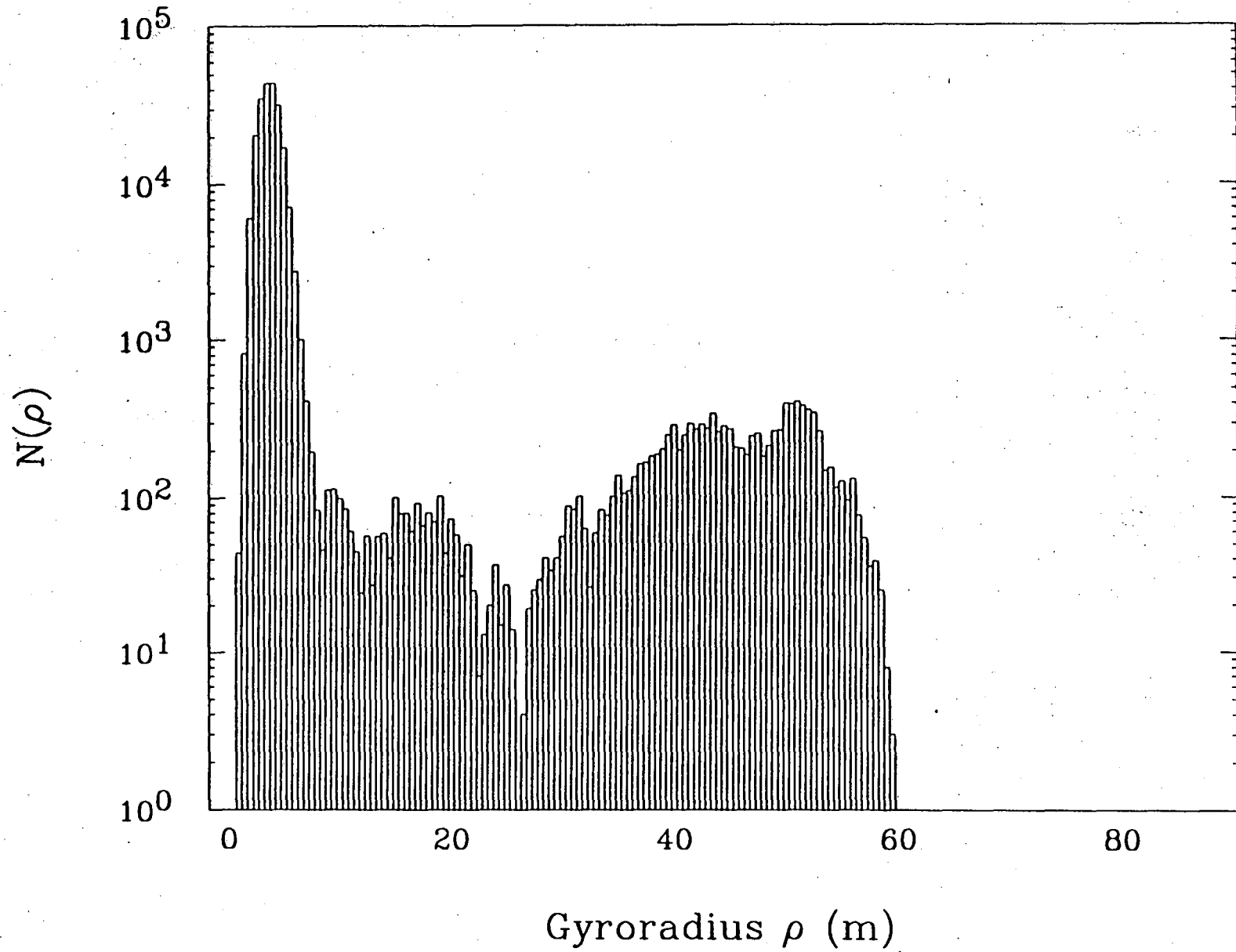

Gyroradius ρ (m)

Fig. 23

Time-Averaged Ion Distribution

Fig. 24

Time-Averaged Ion Distribution
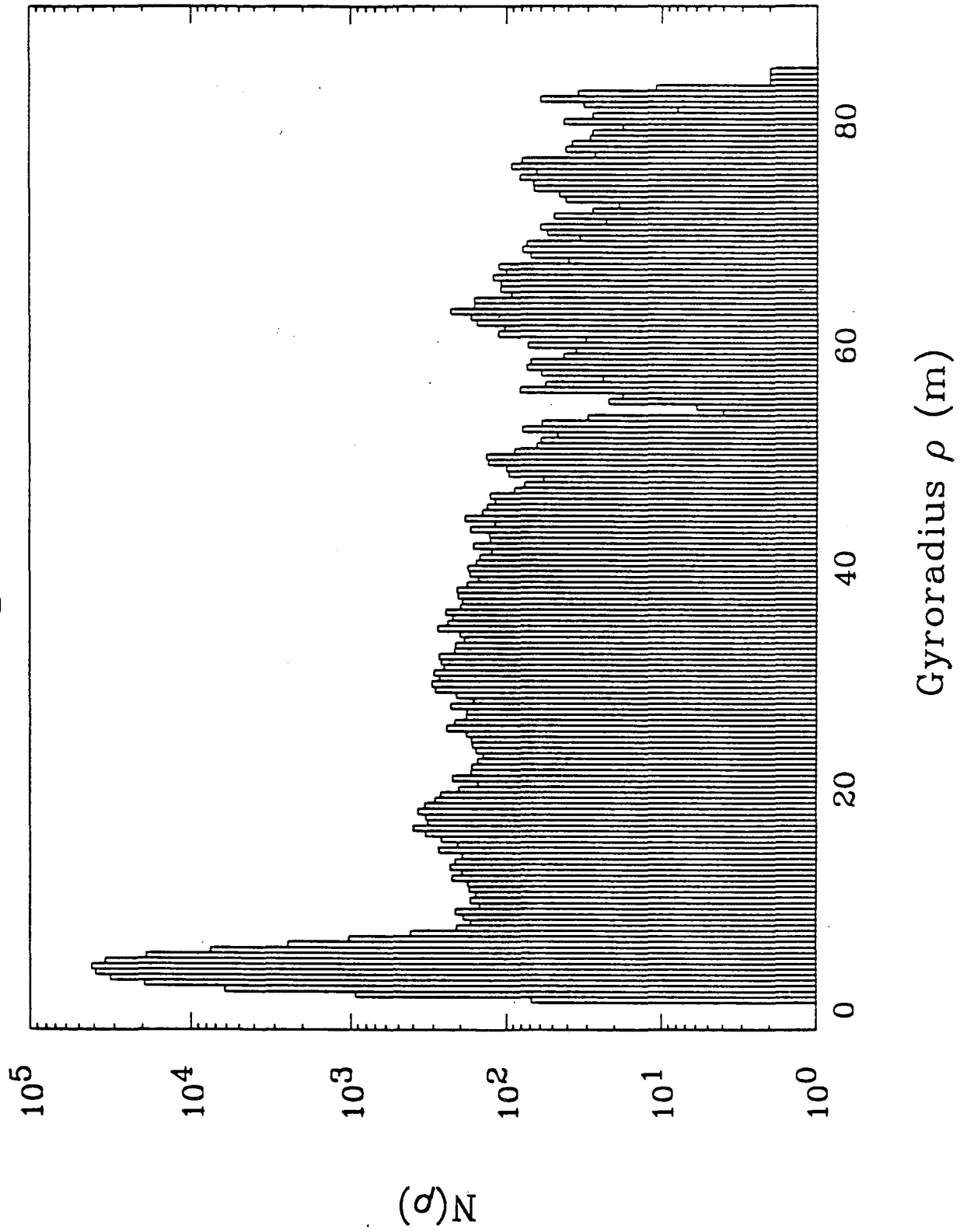

Fig. 25

Time–Averaged Ion Distribution

Gyroradius ρ (m)

$N(\rho)$

Fig. 26

51

Time−Averaged Ion Distribution

Gyroradius ρ (m)

$N(\rho)$
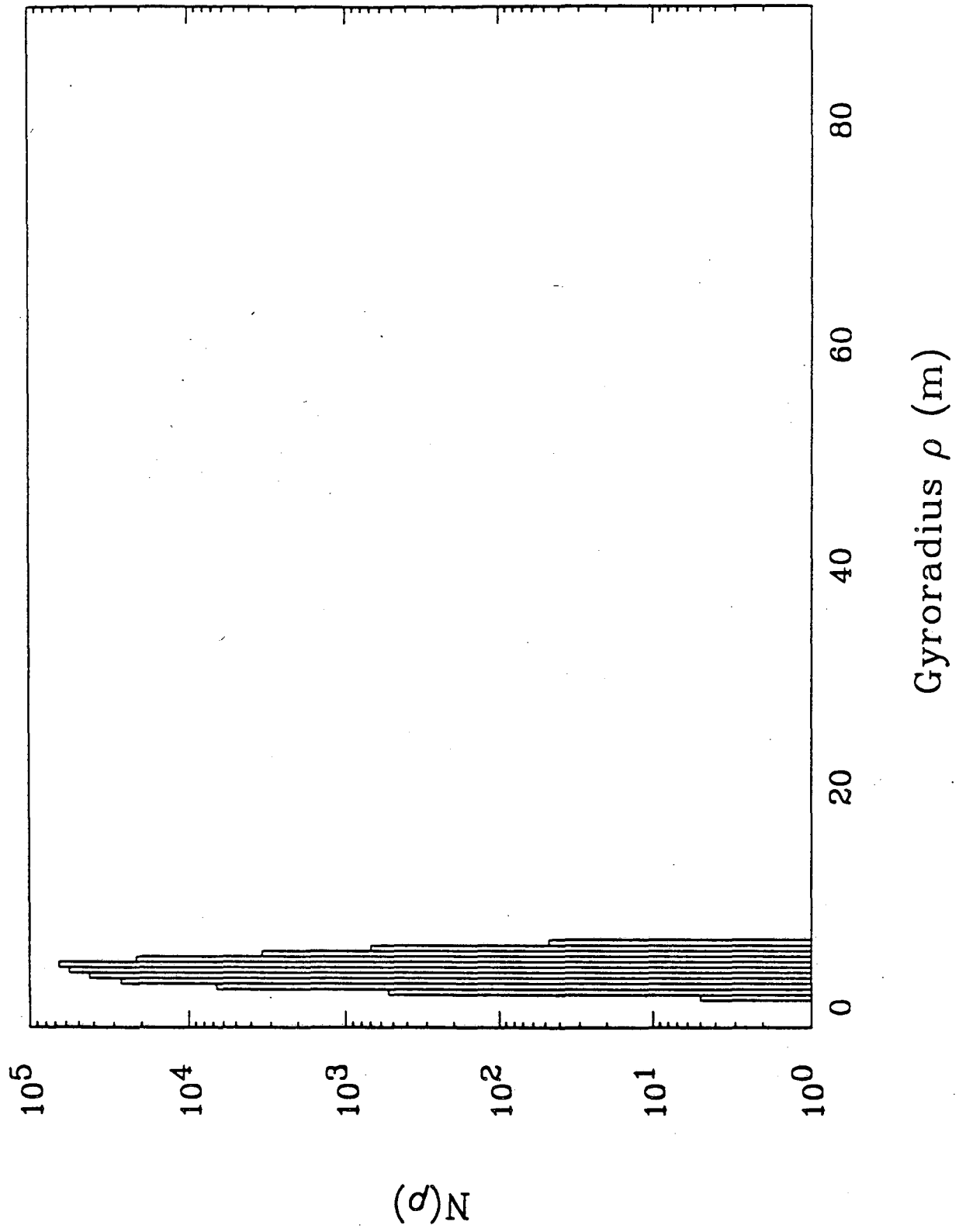
Fig. 27

Time−Averaged Ion Distribution

Gyroradius ρ (m)

Fig. 28

Time-Averaged Ion Distribution

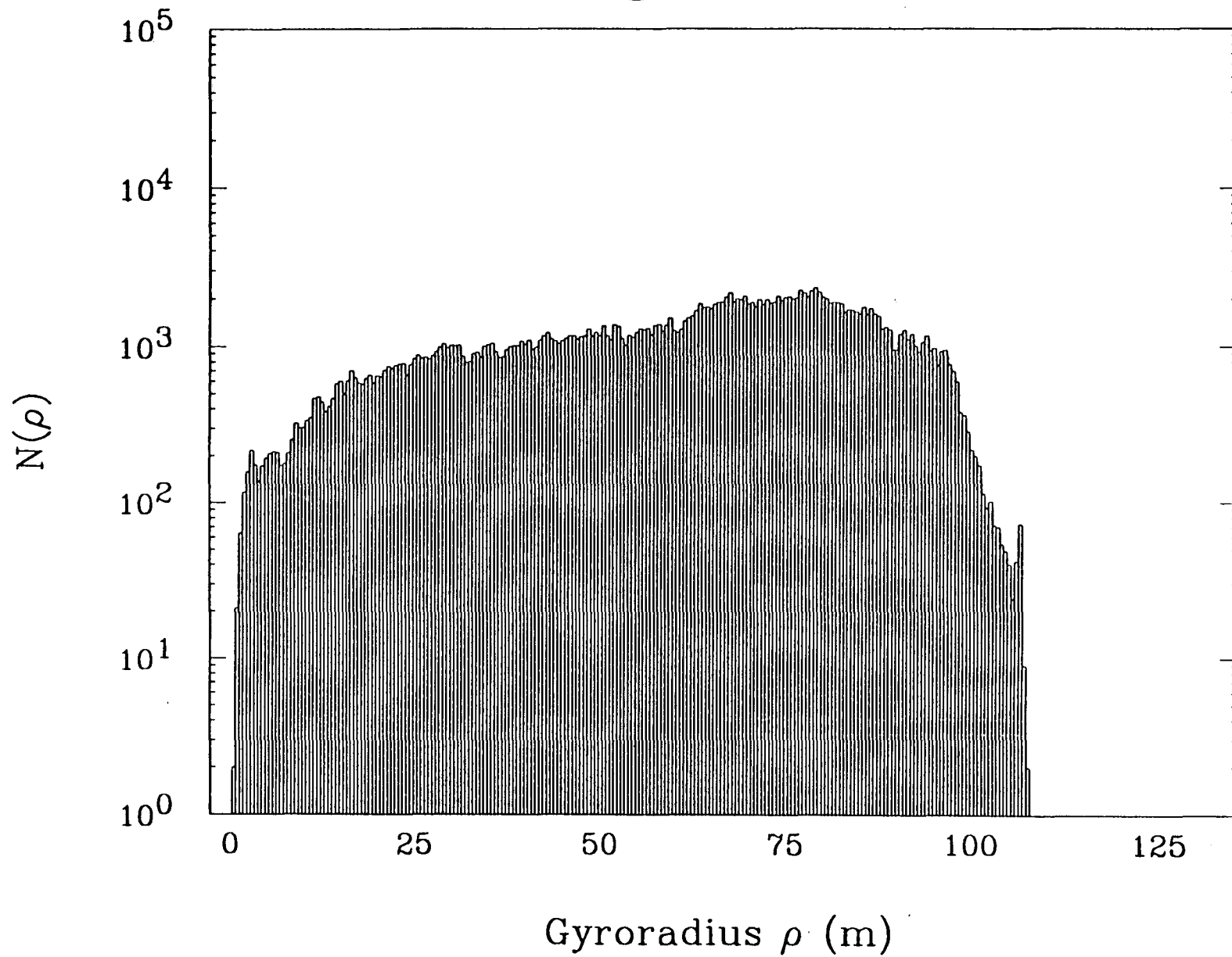Fig. 29
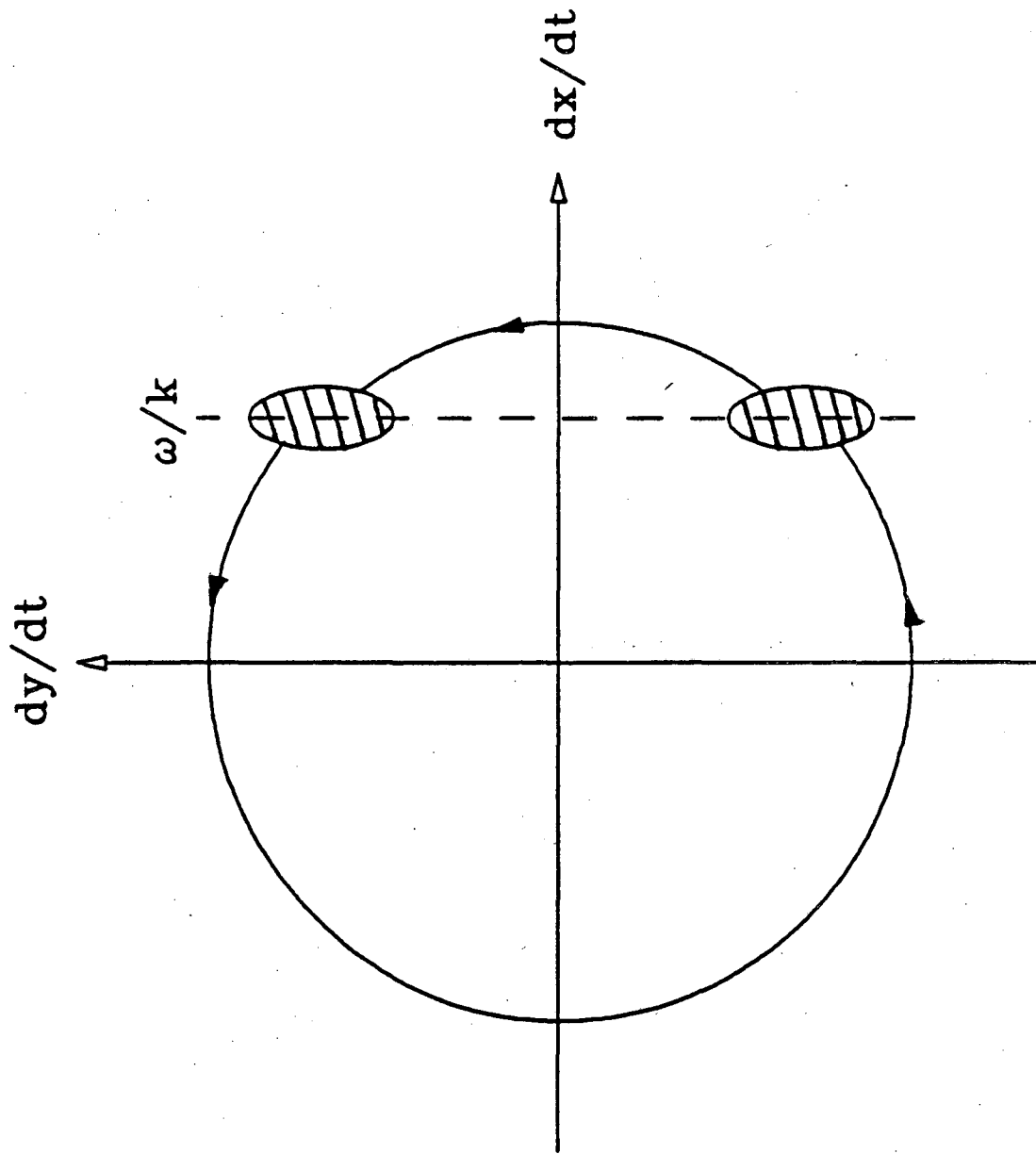
Time–Averaged Ion Distribution

Fig. 30

Fig. 31

56

LAWRENCE BERKELEY LABORATORY
UNIVERSITY OF CALIFORNIA
INFORMATION RESOURCES DEPARTMENT
1 CYCLOTRON ROAD
BERKELEY, CALIFORNIA 94720